Battery-Free Wireless Imaging of Underwater Environments

by

Waleed Akbar

Submitted to the Program in Media Arts and Sciences, School of Architecture and Planning
in partial fulfillment of the requirements for the degree of

Master of Science

at the

MASSACHUSETTS INSTITUTE OF TECHNOLOGY

September 2022

© Massachusetts Institute of Technology 2022. All rights reserved.

Author .....
Program in Media Arts and Sciences, School of Architecture and Planning
August 18, 2022

Certified by .....
Fadel Adib
Associate Professor
Thesis Supervisor

Accepted by .....
Tod Machover
Academic Head, Program in Media Art and Sciences

Battery-Free Wireless Imaging of Underwater Environments

by

Waleed Akbar

Submitted to the Program in Media Arts and Sciences, School of Architecture and Planning
on August 18, 2022, in partial fulfillment of the
requirements for the degree of
Master of Science

Abstract

Imaging underwater environments is of great importance to marine sciences, ocean sustainability, climatology, defense, marine robotics, geology, space exploration, and global food security. Despite advances in underwater imaging, most of the ocean and marine organisms remain unobserved and undiscovered. Existing methods for underwater imaging are unsuitable for scalable, long-term, in situ observations because they require tethering for power and communication. Here we describe underwater backscatter imaging, a method for scalable, real-time wireless imaging of underwater environments using fully-submerged battery-free cameras. The cameras power up from harvested acoustic energy, capture color images using ultra-low-power active illumination and a monochrome image sensor, and communicate wirelessly at net-zero-power via acoustic backscatter. We demonstrate the potential of this method in wireless battery-free imaging of animals, plants, pollutants, and localization tags in enclosed and open-water environments. The method's self-sustaining nature makes it desirable for massive, continuous, and long-term ocean deployments with many applications including marine life discovery, submarine surveillance, and underwater climate change monitoring.

Thesis Supervisor: Fadel Adib
Title: Associate Professor

This thesis has been reviewed and approved by the following committee members:

Prof. Fadel Adib .....
Associate Professor
Program in Media Arts and Sciences, MIT

Prof. Joseph A. Paradiso .....
Professor
Program in Media Arts and Sciences, MIT

Lee E Freitag .....
Principal Engineer
Woods Hole Oceanographic Institution

To Saima, my mentor, guide, and dearest friend.

Acknowledgments

First and foremost, I would like to thank my advisor, Fadel Adib, for his immense support and guidance throughout this research. His vision, optimism, and encouragement made this thesis possible.

I would also like to thank my thesis readers, Lee Freitag and Prof. Joe Paradiso, for their feedback and suggestions. Additionally, I would like to extend my gratitude to Dr. Andrew Bennett for allowing me to use the lab facilities at MIT Sea Grant, and for his insightful suggestions that helped me during testing and experiments.

I am deeply grateful to my collaborators Saad and Osvy, who contributed equally to this research project, for making this work possible with their brilliance, hard work, and enthusiasm. Additionally, I am also thankful to my other collaborators, Mario, Reza, and Unsoo, for their intellectual ideas and exceptional contributions.

I am also grateful to my amazing and fun-loving Signal Kinetics labmates and friends, Laura, Tara, Nazish, Maisy, Aline, Reza, Osvy, Isaac, Saad, Jack, Unsoo, and Purui, for making the lab feel like a home away from home. Over the past two years, I have learned alot from each one of them, and they made my master's degree a memorable experience. I would also like to thank our group admins, Aimee and Holly, for taking care of equipment orders and all other logistical support.

Finally, I would like to express my sincere gratitude to my parents, Akbar and Shazia, and my siblings, Nayyab, Nabeel, and Ayesha, for their unconditional love, unparalleled support, and loads of Duas throughout my whole life. Their kindness, empathy, and belief in my abilities helped me grow personally and professionally. I am also thankful to my dear friends, Buddy, Aamina, Rafae, Momina, Haniya, Sage, Anoosha, Sohail, and Nazish, for supporting me during my low days and listening to my academic and non-academic rants.

This thesis is a revision of a manuscript that appears in Nature Communication (2022). The research is supported by the Office of Naval Research, the National Science Foundation, the Sloan Research Fellowship, the MIT Media Lab, and the MIT Sea Grant.

Contents

List of Figures

List of Tables

Chapter 1

Introduction

Underwater images of marine animals, plants, oceanic basins, coral reefs, and marine debris are key to understanding marine environments and their impact on the global climate system [42, 41, 46, 31]. Underwater imaging enables the discovery of new marine species and advances our understanding of the impact of climate change and human activity on the underwater world [42, 12, 32]. Underwater imaging also supports global aquaculture food production, the world's fastest-growing food sector, where it is used to detect diseases such as sea lice, monitor harmful algae blooms, and regulate fish feeding patterns to optimize growth [13, 62]. More generally, underwater imaging has a large number of applications across oceanography, marine biology, underwater archeology, climatology, space exploration, sustainability, robotics, and defense [39, 33, 34, 63, 26, 5, 28, 7].

Despite advances in underwater imaging, studies estimate that most of the ocean and marine organisms have not been observed yet [40, 24, 11]. A long-standing impediment for underwater observations stems from the difficulty of long-term, real-time, in situ imaging of underwater environments. Existing methods for continuous underwater imaging need to be tethered to ships, underwater drones, or power plants for power and communication [32, 48, 60, 36, 9]. In the absence of such tethering, they rely on batteries which inherently limit their lifetime (and require expensive oceanographic missions for battery replacement). In principle, one could overcome this limitation and power up underwater cameras by harvesting energy from ocean

waves, underwater currents, thermal gradients, or sunlight [9, 65, 57, 61, 27]. However, adding a tidal, solar, or wave harvester to each underwater camera would make it significantly more bulky and expensive, and may limit its deployment environment (for example, solar and wave harvesters work well only near the surface). As a result, it remains challenging today to perform sustainable, continuous, and distributed underwater imaging.

Here, we report underwater backscatter imaging, a battery-free wireless imaging method for underwater environments. Our imaging method is an asymmetric system where an acoustic projector with an active power source wirelessly interrogates and collects image data from a remote battery-less imaging platform. Our imaging platform consumes five orders of magnitude less power than previously reported underwater wireless imaging systems [16, 64, 56]. The ultra-low-power nature of our imaging sensor enables it to operate entirely based on harvested energy. Independence of batteries enables long-term, in situ imaging of remote underwater objects, and wireless communication enables real-time monitoring of underwater environments. As a result, this method may be deployed at scale to discover rare species and observe marine populations, act as early warning systems for diseases in aquaculture farms, monitor geological processes (such as submarine volcanoes) and changes in ocean currents, and more closely surveil commercial and military operations [40, 36, 17].

Our method encompasses fully-integrated ultra-low-power operations including optical sensing, active illumination, processing, and wireless communication. It is capable of performing passive imaging as well as active color imaging using ultra-low-power active illumination, which enables it to operate in different lighting conditions, including complete darkness. Captured images are communicated to a remote receiver that uses them to reconstruct color images of underwater environments. This method can be powered by energy harvested from external sources, such as acoustic, solar, thermal, or ocean current energy. We implement acoustic energy harvesting because of its high efficiency, low cost, and capacity for long-range propagation in underwater environments [53]. The same approaches to energy-neutral imaging can be realized with other sources of ambient energy, such as solar, thermal, or ocean current energy.

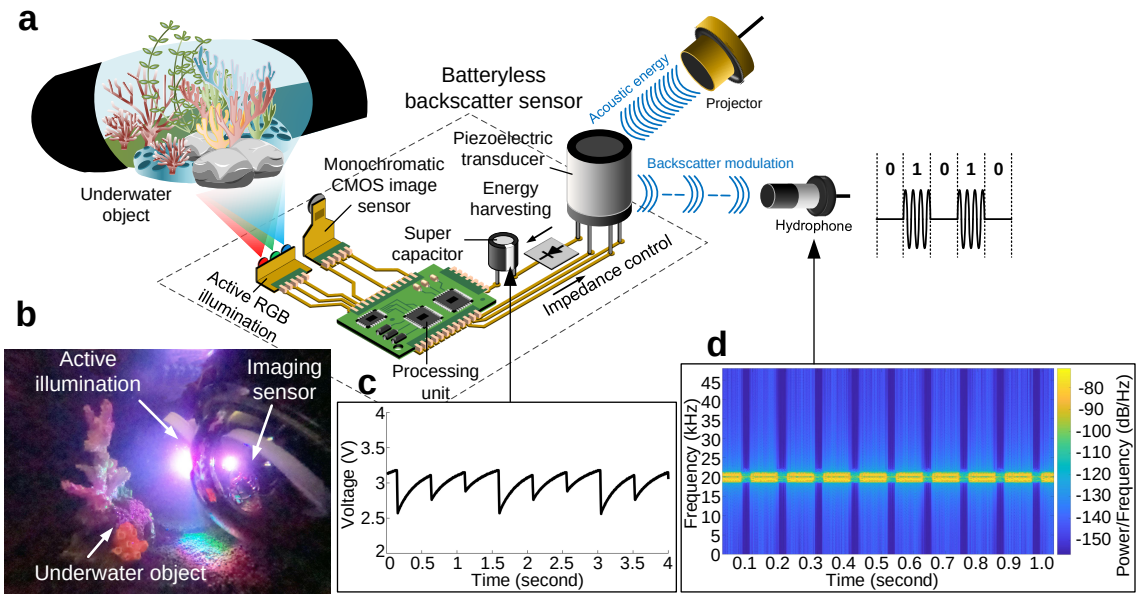

Figure 1-1: **Overview of underwater backscatter imaging.** (a) A remote acoustic projector (top right) transmits sound on the downlink. The acoustic energy is harvested by a piezoelectric transducer and converted to electrical energy that powers up the batteryless backscatter sensor node. The energy accumulates in a super-capacitor that powers up an FPGA unit, a monochromatic CMOS sensor that captures an image, and three LEDs which enable RGB active illumination. The captured image is communicated via acoustic backscatter modulation on the uplink, and a remote hydrophone measures the reflection patterns to reconstruct the transmitted image. (b) The batteryless sensor is shown in an experimental trial where it is used to image an underwater object with active illumination that enables capturing color images. (c) The plot shows the voltage in the supercapacitor, which is harvested from acoustic energy and varies over time as a function of the power consumption of different processing stages. (d) The spectrogram shows the frequency response of the signal received by the hydrophone over time, demonstrating its ability to capture reflection patterns due to backscatter modulation and decode them into binary to recover the transmitted image.

Figure 1-1a schematically summarizes the key components of this wireless imaging method. In acoustically-powered underwater backscatter imaging, a remote projector transmits an acoustic signal on the downlink. Our battery-free sensor node harvests energy from the received acoustic signal using piezoelectric transducers. The received acoustic energy is converted to electrical energy, rectified using a full-wave rectifier, and stored in a super-capacitor. When the stored energy reaches a minimum required threshold, it autonomously activates a power management unit to regulate

the voltage and supply it to an on-board processing and memory unit (realizable as a field-programmable gate array or FPGA) and ultra-low-power oscillators. The processing unit and oscillator trigger an ultra-low-power monochromatic CMOS camera and on-board active illumination to capture the image of an underwater object (Figure 1-1b). The entire imaging process is powered by the harvested energy in the super-capacitor, whose stored voltage varies over time as a function of the power consumption of different processing stages (Figure 1-1c).

A critical step toward realizing battery-free imaging is the development of a technique for ultra-low-power underwater communication. Specifically, the communication component of the system must not consume more energy than what can be harvested from the remote acoustic source, which typically ranges from a few tens to hundreds of microwatts (see Section 3.1). However, state-of-the-art low-power underwater communication modems require 50-100 milliwatts to communicate over tens of meters [50]. Thus, they would require three to five orders of magnitude more power than what is available from harvesting. This significant energy imbalance would make battery-free operation with these modems impractical.

To operate within the energy harvesting constraints of our proposed battery-free imaging method, we leverage piezo-acoustic backscatter to communicate the captured image on the uplink, extending a recently developed net-zero power communication technology [29, 21] to enable telemetry of imaging data. Underwater piezo-acoustic backscatter communicates messages by modulating the reflection coefficient of its piezoelectric transducer (Figure 1-1a). Specifically, due to the electromechanical coupling between a piezoelectric transducer and its electrical impedance load, it is possible to modulate the transducer's radar cross section. Thus, the battery-free node encodes pixels into communication packets by switching between different electric loads (inductors) connected to the transducer. The switching is done by simply controlling two transistors and is realizable with 24 nanowatts of power. A remote hydrophone measures the received acoustic signal to sense changes in the reflection patterns due to backscatter (Figure 1-1d). The reflection patterns are decoded and used to reconstruct the image captured by the remote battery-free cameras. Robust

end-to-end communication is realizable by implementing a full networking and communication stack that incorporates underwater channel estimation, packetization, and error detection.

Our method is capable of capturing color images of underwater objects at ultra-low

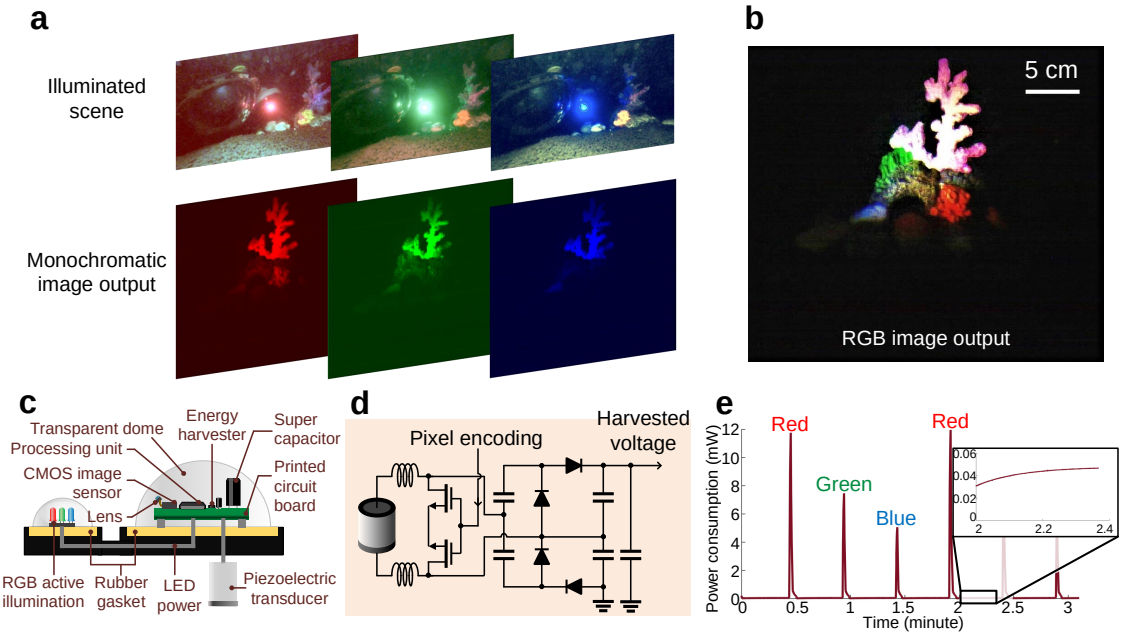

Figure 1-2: **Active illumination in underwater backscatter imaging.** (a) To recover color images with a monochrome sensor, the camera alternates between activating three LEDs - red, green, and blue. The top figures show the illuminated scene, while the bottom figures show the corresponding captured monochromatic images, which are transmitted to a remote receiver. (b) The figure shows the color image output synthesized by the receiver using multi-illumination pixels which are constructed by combining the monochromatic image output for each of the three active illumination LEDs. (c) A side view of the camera prototype demonstrates a larger dome which houses the CMOS image sensor and a smaller dome which contains the RGB LEDs for active illumination. The structure is connected to a piezoelectric transducer. (d) The circuit schematic demonstrates how the imaging method operates at net-zero power by harvesting acoustic energy and communicating via backscatter modulation. (e) The plots show the power consumption over time. The power consumption peaks during active imaging and drops when the captured images are being backscattered.

power even in low-lighting conditions, which are standard in the deep sea due to light absorption in the water column. To do so, we utilize an ultra-low-power CMOS imaging sensor (HM01B0 from Himax Corporation), which can capture monochromatic images. To reconstruct color images using the monochromatic imaging sensor,

we devised a method for low-power multi-color active illumination. Our battery-free imaging system incorporates three monochrome light emitting diodes (LEDs): red, green, and blue. An ultra-low-power processing and memory unit (IGLOO nano FPGA) alternates between activating each of these LEDs and captures monochromatic images with each active illumination cycle (Figure 1-2a). The monochromatic images are acoustically backscattered to the remote receiver. After decoding each of the images, the receiver synthesizes the received packets into multi-illumination pixels by applying them to the RGB channels of a digital pixel array to reconstruct color images, demonstrating the possibility to recover color patterns of underwater objects such as corals (Figure 1-2b).

We demonstrate that in situ underwater wireless batteryless imaging is possible using a self-powered camera system (Figure 1-2c) that harvests acoustic energy and communicates using piezo-acoustic backscatter (Figure 1-2d). The harvested energy is expended in cycles that alternate between imaging and communication (Figure 1-2e). Upon capturing image segments, the processing unit packetizes the pixels and communicates them using piezo-acoustic backscatter, at a power consumption of 59 μW. To deal with the bandwidth mismatch between the ultra-low-power CMOS image sensors (few Mbps) and the underwater acoustic communication channel (few kbps), the captured images are buffered in the memory unit cells. Our fabricated opto-electro-mechanical system consists of multilayer piezo-electric transducers, electronic components (diodes, capacitors, low-power voltage regulators, and DC-DC converters, low-power oscillators), a processing and memory unit (FPGA), LEDs, and a CMOS image sensor. Active illumination using the LEDs is the most power consuming operation of the battery-free imaging system. For acoustic communication rates of 1 kbps, empirical measurements demonstrate an average power consumption of 276.31 μW for active imaging. In our demonstrations of passive monochromatic imaging where active illumination isn't needed, the batteryless camera consumes an average of 111.98 μW. In both configurations, the entire energy budget is harvested from underwater acoustics. Other configurations with different throughput and active illumination techniques are possible.

We built a proof-of-concept prototype to demonstrate underwater backscatter imag-

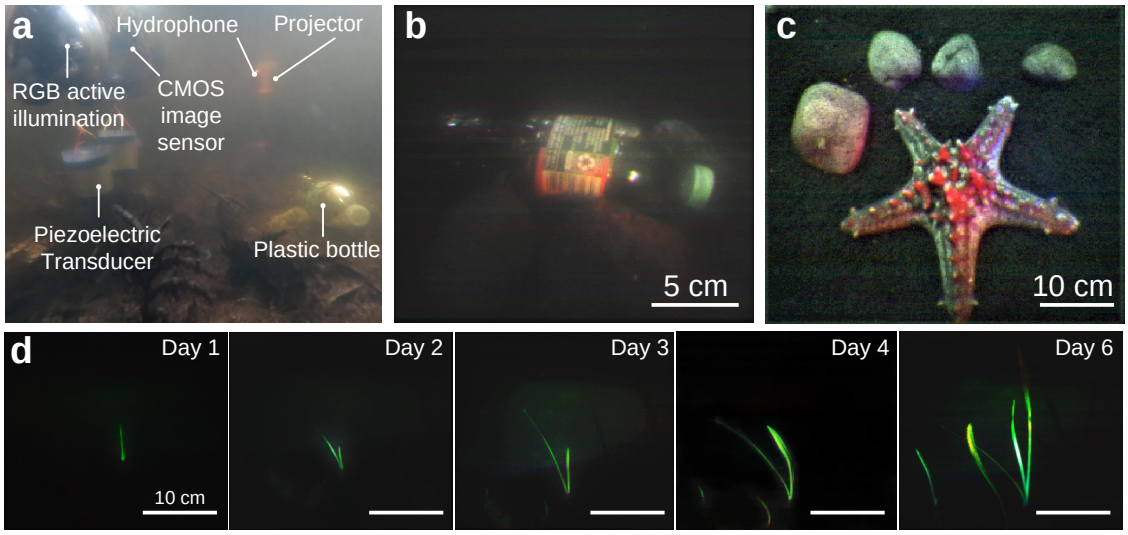

Figure 1-3: **Sample images obtained using underwater backscatter imaging.** (a) The figure shows a photo of a prototype deployed in Keyser Pond for monitoring pollution from plastic bottles on the lakebed. (b) The RGB image output obtained from the imaging method while monitoring pollution in Keyser Pond. (c) RGB image output for *Protoreaster linckii*, demonstrating qualitative success in recovering its color and numerous tubercles along the starfish's five arms. (d) The imaging method was used to monitor the growth of an *Aponogeton ulvaceus* over a week. The figures show the captured images on different days of the week.

ing with animals, plants, and pollution across controlled and uncontrolled environments. The prototype was tested in Keyser Pond in southeastern New Hampshire (43°N, 72°W), where it was used to image pollution from plastic bottles on a lakebed at 50 cm from the imaging sensor (Figure 1-3a). Here, color imaging using a monochromatic sensor was successful (Figure 1-3b), despite the presence of external illumination. The prototype was also successful in imaging the *Protoreaster linckii*, also known as the African starfish, in a controlled environment with external illumination; the captured image displays numerous tubercles along the starfish's five arms (Figure 1-3c). Furthermore, due to the ability of underwater backscatter imaging to operate continuously, the method was successful in monitoring the growth of an *Aponogeton ulvaceus*, where imaging was performed in the dark over a week, while relying entirely using the harvested energy and active multi-color illumination (Figure 1-3d). In all of these scenarios, the prototype was fully-submerged, wireless, batteryless, and au-

tonomous.

The benefits of underwater backscatter imaging extend beyond observational monitoring to more complex tasks such as underwater localization and inference. To demonstrate the feasibility of such tasks, the imaging method was used to detect and localize visual tags such as AprilTags; these tags have been previously utilized for underwater localization and robotic manipulation [14, 10]. Our evaluation results show that the imaging method can achieve very high detection rate and high localization accuracy (localization error below 10 cm) up to 3.5 m. We also evaluated the method's harvesting and communication capabilities as a function of distance in the Charles River in eastern Massachusetts (at 42°N, 71°W). Our results demonstrate the ability of the system to robustly decode packets beyond 40 meters by leveraging a decision feedback equalizer (DFE) at the receiver [20]. These results show that underwater backscatter imaging is a viable batteryless telemetry method and that higher ranges may be realizable with higher levels of underwater acoustics or by leveraging underwater transducers with higher efficiency [2] (see Section 3.1).

In summary, this work demonstrates that wireless battery-free imaging in underwater environments is possible. Our method encompasses a highly efficient underwater color camera and innovations that enable robust acoustic backscatter communication in practical underwater environments. The tetherless, inexpensive, and fully-integrated nature of our method makes it a desirable approach for massive ocean deployments. Scaling the method for large-scale deployments requires more sophisticated underwater transducers or high-power underwater acoustic transmissions. Its scalability may be further enhanced by leveraging a mesh network of buoys like those already being deployed on the ocean surface, networks of subsea robots like Argo floats, or surface vehicles like ships to remotely power the energy-harvesting cameras [59, 47]. Massive deployments would enable tracking undersea movements - including the flow of particulate organic carbon [44], marine animals, and naval assets - at scales not realizable today. These may be used to create more accurate models capable of monitoring climate change [19], decrease the stealthiness of nuclear submarines through large scale observations, and advance various marine scientific fields.

Chapter 2

Methods

2.1 Communication through backscatter

To enable ultra-low-power communication, our batteryless sensor employs piezo-acoustic backscatter [29]. Piezo-acoustic backscatter differs from traditional underwater acoustic communication in that it does not need to generate its own acoustic signal to communicate. Instead, it communicates by modulating the reflections of incident underwater sound, and a remote receiver can decode the transmitted data by recovering patterns in the reflected signals.

To transmit the stored image data via piezo-acoustic backscatter, our prototype uses two N-channel MOSFETs to modulate the impedance across the terminals of an underwater transducer. The design uses these MOSFETs to switch the transducer's reflectivity between two states similar to prior underwater backscatter designs [29, 21, 1]. The signal-to-noise ratio (SNR) at the receiver is maximized when the complex-valued difference (i.e., amplitude and phase) between the two reflective states is maximum. Through our empirical analysis, we have observed that a high SNR on the uplink channel is achieved when the node switches between an inductively matched load and an open circuit. Hence, the FPGA controls the switch to alternate the load between an open circuit and the inductive load to send image data using bi-phase space encoding modulation (also known as FM0) which is known to have high noise resilience in time-varying channels [4]. Other modulation and coding schemes are also possible.

2.2 Uplink decoding

The backscatter communication signal is received by the hydrophone and decoded using a robust demodulation and decoding pipeline (figure 2-1) that is implemented through offline packet processing.

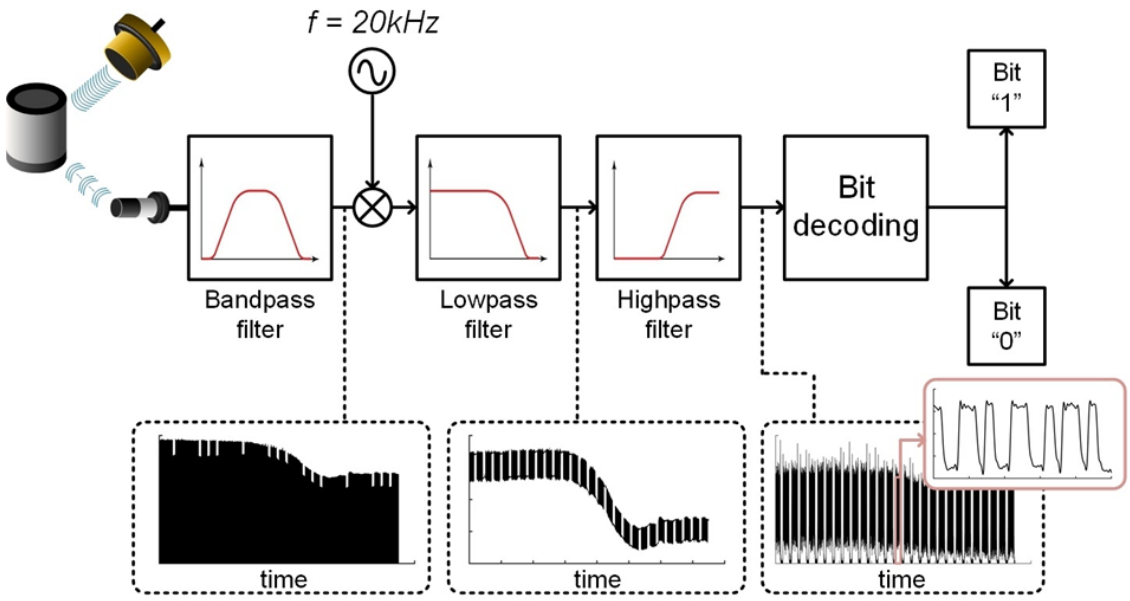

Figure 2-1: **Demodulation and decoding pipeline.** The signal received by the hydrophone is passed through a band-pass filter, then downconverted and passed through a low-pass filter to remove noise. This signal is then passed through a high-pass filter to remove the signal variations caused by low-frequency surface waves. The demodulated and filtered signal is fed to a maximum likelihood decoder.

The demodulation pipeline consists of a series of filters followed by a maximum likelihood decoder. To remove noise from the received signal, we use a bandpass filter centered around the carrier frequency of 20 kHz with a passband of 10 kHz from 15-25 kHz (the filter is implemented as a linear phase type 1 discrete-time FIR filter with filter length of 297). After the bandpass filter, we downconvert the passband signal to baseband by multiplying it with the carrier frequency (20 kHz sinusoid), then use a low pass filter with a bandwidth of 4 kHz (a linear phase type 1 discrete-time FIR filter with filter length of 347, and 6 kHz stopband frequency) to remove high-frequency components from the signal. To mitigate low-frequency interference from naturally-occurring surface waves and turbulence, we implement a high-pass filter (a

linear phase type 1 discrete-time FIR filter with filter length of 4535; the respective passband and stopband frequencies of the filter are 150 Hz and 20 Hz). These filtering stages enable the receiver to operate correctly in uncontrolled and time-varying underwater environments.

After filtering and demodulation, the receiver proceeds to packet detection. Each backscatter packet starts with a preamble, and each image segment is sent over multiple packets (as discussed in the subsequent section on FPGA control and logic). The receiver correlates the raw received signal with a known preamble sequence to detect the beginning of the packet. After packet detection, the receiver proceeds to decoding the FM0-encoded packets in baseband. We implemented a bit-by-bit maximum likelihood decoder that has high resilience to channel variations. Formally, consider a received FM0 symbol of size n $\mathbf{x} = x_0, x_1, ..., x_{n-1}$. The decoding operation is done in two steps. The first step performs mean subtraction, exploiting the fact that each FM0 encoded bit has zero mean with respect to neighboring half bits. Mean subtraction removes the constant self-interference signal from the projector as well as any hardware offsets at the receiver. The mean-subtracted symbol $\mathbf{x}^{'}$ can be expressed as:

$$\mathbf{x}^{'} = \mathbf{x} - \frac{1}{2n} \sum_{i=-\frac{n}{2}}^{n+\frac{n}{2}-1} x_i$$

The second step is maximum likelihood decoding, which is performed by projecting the mean-subtracted received symbol on the time-series symbols $\mathbf{y^0}$ and $\mathbf{y^1}$, which represent bits 0 and 1 respectively, as per the equation:

$$b = \arg\max_{k=0,1} (\sum_{i=0}^{n-1} \frac{y_i^k x_i^{'}}{\|x\|^2})$$

Once a packet is decoded, a packet sequence number is used to identify if any of the packets were missed or dropped during the communication process, and a parity bit helps identify incorrectly decoded packet payloads. The packet number and parity check allow the receiver to detect corrupted or missed packets. By incorporating downlink communication, future designs may leverage this capability to request re-

transmissions from the batteryless sensor.

Finally, it is worth noting that while our implementation focused on uplink communication between one camera sensor and a hydrophone receiver, it is possible to extend to this design with downlink communication, multiple sensor nodes, and multiple receivers; it is also possible to implement other packet sequences with alternate headers that include additional addressing and coding schemes similar to prior work on underwater backscatter [29, 21]. Note that the extension of the current imaging platform with narrowband downlink communication would only take minimal energy (as shown in the prior work [29]) and therefore, it would add little to the overall power consumption of the system.

2.3 Energy harvesting and power management

To operate at net-zero power, the batteryless underwater camera sensor may harvest sufficient energy from a remote acoustic source. We use an underwater projector that transmits a 20 kHz sinusoidal acoustic signal (source level 180 dB re 1 μPa @ 1 meter) on the downlink [1]. The transmitter uses a layered transducer node to convert the input electrical sinusoidal wave to an acoustic wave.

The transmitted acoustic signal propagates underwater and reaches our batteryless sensor. On the sensor side, a harvesting transducer converts the mechanical vibrations, which are due to pressure changes of the incident acoustic signal, into an electrical sinusoidal signal that can be used to power the circuit. Since the electrical signal produced by our transducer is an alternating current signal, it first needs to be rectified. In our design, the outer layer of the harvesting transducer is directly connected to the harvester circuit; the harvester circuit is composed of an impedance matching network that ensures maximum power transfer efficiency and a four-stage voltage multiplier that rectifies the incoming differential input voltage and quadruples the rectified DC voltage (figure 2-2). The rectifier utilizes Schottky diodes with

[1] The projector has a toroidal radiation pattern and consumes 25 W of power to achieve a source level of 180 dB re 1 μPa @ 1 meter (see Sections 4.1 and 3.1). The power consumption of the transmitter can be reduced by using a directional transducer.

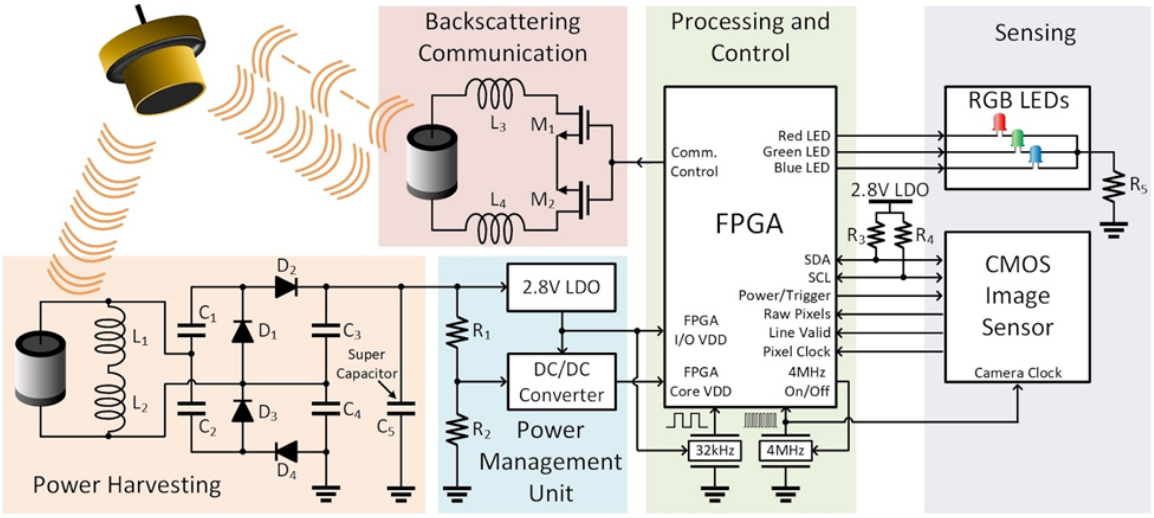

Figure 2-2: **Schematic of the hardware design.** The harvester node at the bottom is connected to a multi-stage rectifier followed by a supercapacitor, which stores the harvested energy. The supercapacitor voltage is fed to a 2.8V LDO and to a 1.4V DC/DC step-down converter. The output of the DC/DC converter is used to power the FPGA core, and the output of the LDO is used to power the FPGA banks. The FPGA is also connected to two external clocks (32kHz and 4MHz) and to the camera via several GPIO pins (pixel clock, line valid, data, power, master clock). The FPGA controls the operation of the MOSFETs connected to the communication transducer on the top left. This transducer is responsible for sending camera data via backscatter communication.

a maximum forward voltage of 350 mV. This rectified voltage is then fed into a super capacitor. The super capacitor's output voltage is regulated by a 2.8 V Low Dropout (LDO) which drives digital components such as the bank voltage of the FPGA and two external clocks (32 kHz and 4 MHz). The LDO is connected to a DC-DC step down converter, which steps down its 2.8 V to 1.4 V. This allows running the Himax camera and oscillators at their required voltages while running the FPGA core at 1.4 V to minimize power consumption.

In principle, the regulated voltage can be directly used to power up the rest of the sensor electronics and bootstrap the image capture operation and communication. In practice, however, the harvested power may be less than that required to run the electronics for an entire imaging cycle. This is particularly true when the sensor is further away from the projector, leading to a lower harvested power than that required for imaging. In such scenarios, if the capacitor were to provide energy to the rest of the

electronic components prematurely, they would drain its energy and abruptly shut down the circuitry before it can capture an image segment.

To ensure that the rest of the circuit does not power up prematurely, our method incorporates a cold-start phase where it harvests energy in its super-capacitor before it powers on the rest of the circuit electronics. To implement this cold-start phase, our design leverages the DC-DC step down converter as a power-gating mechanism (i.e., as a way to buffer energy before providing it to the rest of the circuit), exploiting the fact that the DC-DC converter controls the core voltage of the FPGA logic unit. To do this, our design uses a potential divider to feed a portion of the capacitor voltage to the "enable" pin of the DC-DC step down, so that the DC-DC activates when the capacitor voltage reaches a desired voltage (e.g. 3.2 V in our design). This allows our circuit to harvest energy for a sufficient period of time before it starts operation. Additionally, once the DC-DC turns on, it does not turn off until the enable pin voltage falls below a minimum threshold voltage (e.g.,1.4 V in our design). In other words, hysteresis allows the DC-DC to stay active even when the voltage at the enable pin is fluctuating over a wide range. The fluctuation in voltage typically happens due to two main reasons: the first is the variations in harvested energy (from sound) due to the changing underwater channel, and the second is the variation in current draw from various on-board components during different phases of operation (as described in subsequent sections on FPGA control and logic and on Power analysis).

Finally, we discuss how the capacitance (C) of 7500 μF and minimum threshold value (V_{thres}) of 3.2 V are determined. Since the camera sensor requires a minimum voltage (V_{min}) of 2.8 V for reliable operation, the design of the batteryless sensor must ensure that the capacitor voltage remains above V_{min} when the camera is operational. Conservatively, the super-capacitor needs to store enough energy to power the circuit for capturing an entire image segment before the energy drawn causes the voltage to drop below V_{min}; this analysis is conservative since the sensor continues harvesting even during the imaging phase. Mathematically, we can express this energy buffer as:

$$EnergyBuffer \geq \frac{1}{2}CV_{thres}^2 - \frac{1}{2}CV_{min}^2$$

The energy buffer was determined empirically by measuring the energy required by the camera prototype to capture an image segment using active imaging (5 mJ, see subsequent section on Power Analysis). Given that V_{min} is 2.8 V, we can select C = 7500 μF and V_{thres} = 3.2 V to satisfy the above inequality.

Our proof-of-concept implementation employs two separate transducers for harvesting and backscatter communication. In principle, it is possible to use a single transducer - rather than two - for both energy harvesting and backscatter communication, since both transducers are identical. However, doing so would result in less harvested energy; this is because less energy may be harvested in the open-circuit state than in the inductively matched state. Thus, in our prototype implementation, we decouple the communication from the energy harvesting so that both processes can occur simultaneously without either of them reducing the other's efficiency. Alternate implementations with a single transducer for both harvesting and communication, or with multiple transducers for each of harvesting and communication are possible. The latter is useful for enabling longer-range operation since the combination of multiple transducers can harvest more energy and achieve higher SNR on the uplink (both of which increase with the number of transducers used).

2.4 FPGA control and logic

A key challenge in enabling net-zero power wireless underwater imaging arises from the limited communication bandwidth of underwater acoustic communication, which is typically of the order of few kilobits/sec [30]. Due to the limited bandwidth of underwater acoustic channels, the transfer time of underwater images is typically tens of minutes or even hours [23]. In principle, one could keep the CMOS imaging sensor and LED illumination turned on during this period. However, such an approach would be counterproductive since these components consume significantly more power than the rest of the circuit. Here, it is worth noting that higher throughput (thus shorter transfer time) may be realizable using more advanced modulation techniques such as OFDM [38]. However, these techniques require much higher power consumption than

underwater piezo-acoustic backscatter [29].

To enable low-power operation while dealing with the bandwidth constraints of underwater acoustic channels, our method employs an FPGA that operates in two phases: image capture phase (which is power-limited) and backscatter communication phase (which is bandwidth limited). The operation in each of these phases is optimized to minimize overall energy consumption of the underwater backscatter imaging method and enable net-zero operation, as explained below.

2.4.1 Image Capture Phase

Once the super-capacitor has stored sufficient energy from harvesting (e.g., 3.2 V or higher), the voltage at the enable pin of the DC-DC overcomes its threshold, allowing it to power the FPGA core at 1.4 V, as well as the 32 kHz external oscillator. Once the FPGA core is turned on, it initiates its logic sequence to power on the Himax camera sensor along with an external 4 MHz oscillator. The higher frequency clock signal is necessary to operate the camera (which requires at least 3 MHz) and communicate with it over an I2C interface (100 kHz - 400 kHz).

Once all the onboard components are powered on, the interfacing process starts. The FPGA configures the camera sensor through the I2C communication bus, which enables it to set different parameters on the camera sensor - such as the image resolution, exposure level, and data bits sequence - to enable adapting the image capture to different environmental conditions. In our implementation, the FPGA logic first resets the camera sensor, then sets the image resolution to Quarter Video Graphics Array (QVGA) frame with a resolution of 324 by 244 pixels (each pixel is represented by 8 bits for a total of 632,448 bits per image) and specifies the data transfer protocol to be serial (using a single port and sending the most significant bit first). Finally, the FPGA sets the clock of the camera sensor core to be master clock (MCLK) divided by 8, or more specifically, 4 MHz/8 = 0.5 MHz. To set these parameters, the FPGA uses two I2C connections (SDA, SCL), and it receives all necessary information from three distinct pins on the camera sensor: 1) HSYNC (or line valid), a signal that goes high when a row of the image is being sent and is low otherwise, 2) PCLK (the

pixel clock), and 3) DATA0, where the data is transmitted serially. Moreover, the FPGA controls the power to the camera through the power pins (AVDD/IOVDD) (figure 2-2). The CMOS imaging sensor sends an acknowledgement after each I2C instruction, indicating the successful execution of the corresponding instruction.

Upon successful I2C communication, the FPGA powers on the red LED, then instructs the camera sensor to capture an image and initiate data transfer process to the FPGA memory. Due to the limited FPGA on-board RAM size (a total of four 4608-bit blocks), only 12 kbs are saved to memory at a time. The RAM is configured as 256-word-deep FIFO, with 48-bit words. After reaching full memory capacity, the FPGA turns off the camera, LED, and 4 MHz oscillator, and switches to the 32 kHz oscillator as it enters the communication phase where it transmits the stored image segment to the receiver.

2.4.2 Backscatter Communication Phase

During the backscatter communication phase, our FPGA uses the lower frequency oscillator of 32 kHz for reading from the memory and transmitting the stored image data because the data rate is limited to 1 kbps due to the narrow bandwidth of underwater acoustic channels. Additionally, the low frequency oscillator allows the FPGA to operate at extremely low power because its dynamic power consumption decreases with the clock frequency. At 32 kHz, most of the power consumption is static (as opposed to dynamic).

The FPGA encodes the image data into packets (figure 2-3). Each 77-bit-long packet contains a 16-bit preamble, followed by a 12-bit packet number, 48 bits of data, and a single parity bit at the end. Furthermore, to help the decoder identify packet boundaries, the FPGA introduces a brief silent period (equivalent to the time needed to transmit 23 bits) at the end of each packet. The FPGA converts the data bits into FM0 modulation. The FPGA feeds the FM0 encoded data bits to the gate pin of the two MOSFETs to communicate the image data through backscatter.

After each image segment (stored in memory) is sent, the aforementioned process repeats for the same segment but with a different LED turned on (i.e, green and

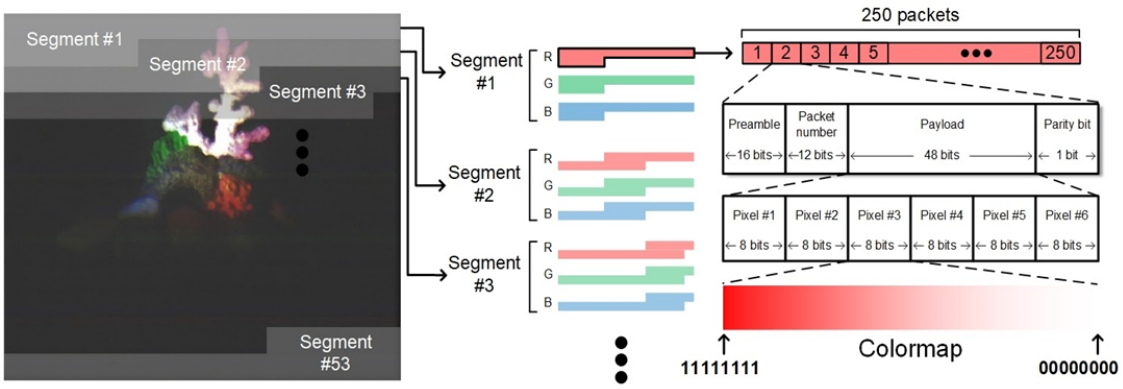

Figure 2-3: **Packetization of pixel data.** The image captured by the CMOS image sensor is divided into 53 segments. Each image segment is divided into 250 packets, where each packet contains data for 6 pixels. The uplink packet structure includes a 16-bit preamble, followed by a 12-bit long packet number, and a payload of 48 bits. A parity bit is appended to each packet; it is set to 1 if the sum of bits in the payload is even and is set to 0 otherwise.

then followed by blue). Once the same image segment is transmitted and received for all three illuminations (RGB), the FPGA stores the next segment of the image and repeats the same process until an entire image is transmitted. The FPGA also stores the segment index in a designated register and uses a counter to wait for 12000*$segment\_index$ clock cycles to store the desired segment to the FIFO memory. The overall process requires 53 repetitions (53 segments per image, due to memory constraints on the FPGA) for monochromatic images and 159 for active color illumination. For FPGAs with larger memory size, the number of repetitions will be lower.

2.5 Power analysis

Our proof of concept prototype can perform active and passive imaging at an overall average power consumption of 276 μW (table 2.1) and 112 μW (table 2.2) respectively. Note that the additional power requirements for active imaging is due to the active illumination, and that the average power is reported over the duration of capturing and transmitting an entire image (i.e., by dividing the total energy consumed across all operation phases by the time to capture and transmit the image).

	Image Capture Phase (700 ms per image segment)		**Backscatter Communication Phase** (25 s per image segment)	
Device Components	**Power Consumption (mW)**	**Energy Consumption (mJ)**	**Power Consumption (mW)**	**Energy Consumption (mJ)**
Camera Sensor	1.1	0.77	0	0
Active Illumination (R,G,B)	(8.22696, 4.391, 2.71)	(5.7588, 3.0737, 1.8977)	0	0
AGLN060 FPGA	0.4807	0.336	0.0224	0.56
4MHz oscillator	0.168	0.1176	0	0
32kHz oscillator	0.0126	0.0088	0.0126	0.3150
DC/DC step-down converter	0.054867	0.0384	0.001244	0.0311
Low dropout (R,G,B)	(1.4372, 1.3127, 0.575233)	(1.00604, 0.91889, 0.4026631)	0.022854	0.57135
N-Channel MOSFETs	0	0	24e-9	6e-7
Average Power Consumption	[Total Energy Consumption (Image Capture Phase) + Total Energy Consumption (Backscatter Communication Phase)]/Total time = [894.2 mJ + 234.91 mJ]/4086.3 s = 0.276 mW = 276.31 μW			

Table 2.1: **Power consumption for active color imaging.** The table shows the power consumption breakdown for each component in the prototype while performing active imaging. The energy consumption is computed and shown separately for each of the image capture and backscatter communication phases. Since there are 53 segments per image and each segment is repeated three times (once for each active illumination), the average power consumption of capturing and communicating an entire color image is 276 μW.

Our method's ultra-low power consumption is realizable due to multiple design factors. First is the use of underwater backscatter communication to transmit pixel data. In contrast to traditional underwater acoustic communication technologies, underwater backscatter does not need to generate its own signal; instead, it communicates by modulating the reflection patterns of incident acoustic signals. The process of switching between the two states requires passive switches (e.g. MOSFETs) which

	Image Capture Phase (700 ms per image segment)		**Backscatter Communication Phase** (25 s per image segment)	
Device Components	**Power Consumption (mW)**	**Energy Consumption (mJ)**	**Power Consumption (mW)**	**Energy Consumption (mJ)**
Camera Sensor	1.1	0.77	0	0
AGLN060 FPGA	0.4807	0.336	0.0224	0.56
4MHz oscillator	0.168	0.1176	0	0
32kHz oscillator	0.0126	0.0088	0.0126	0.3150
DC/DC step-down converter	0.054867	0.0384	0.001244	0.0311
Low dropout	0.1848	0.12936	0.022854	0.57135
N-Channel MOSFETs	0	0	24e-9	6e-7
Average Power Consumption	[Total Energy Consumption (Image Capture Phase) + Total Energy Consumption (Backscatter Communication Phase)]/Total time = [74.234 mJ + 78.304 mJ]/1362.1 s = 0.112 mW = 111.98 μW			

Table 2.2: **Power consumption for passive grayscale imaging.** This table shows the power consumption breakdown for each component of the prototype while performing passive grayscale imaging. The energy consumption is computed and shown separately for each of the image capture and backscatter communication phases. The average power consumption of capturing and communicating an entire grayscale image is 111.98μW.

consume 24 nanowatts of power, making the communication process extremely low power. Second is the use of low-cost commercially available ultra-low-power FPGAs, which consume as little as 22 μW during certain phases of the operation. Third is the switched dual-oscillator method (of 32 kHz and 4 MHz), which allows minimizing the energy consumption by adapting clocking to different phases of operation. Specifically, in the bandwidth-limited phase - i.e., when the method is constrained by the bandwidth of the underwater acoustic channel, the method switches to the low-frequency oscillator (32kHz), minimizing the power consumption of the FPGA. On the other hand, in the power-limited phase - i.e. when the method is limited by the power consumption of the CMOS image sensor (0.77-1.1 mW) and LEDs (1.9-8.2

mW), it switches to the high-frequency clock to rapidly complete the pixel transfer to the FPGA and turn off the camera and LEDs during the communication phase. Since the FPGA switches the high-power components off during communication, the supercapacitor can harvest energy and recharge during that phase. The overall power consumption is optimized through a simple, low-cost, power-management unit with a DC-DC converter, low-power LDOs, and resistor dividers as described earlier. The ultra-low power consumption may be further reduced by duty cycling rather than continuous operation.

Chapter 3

Range & Timing Analysis

3.1 Range Analysis

In battery-free backscatter communication systems, the end-to-end communication range is determined by the ability of a remote transmitter to power up the battery-free sensor [3, 2]. Hence, to understand the communication range of our underwater battery-free imaging system, we analyze the downlink range between the projector and the battery-free node. Our downlink analysis follows a model introduced in recent work that studied the range of underwater acoustic backscatter communication systems [2].

The downlink communication range of our system is determined by two constraints: (a) the harvested power and (b) the rectified voltage. In particular, the harvested power needs to exceed a minimum threshold for continuous operation, and the rectified voltage needs to exceed a minimum activation voltage required to turn on the LDO (see Section 2.3). Since the harvested power and the rectified are both a function of the open-circuit voltage, we first analyze the open-circuit voltage as a function of range, then relate it to the harvested voltage and power.

3.1.1 Open-Circuit Voltage

The voltage at the harvesting transducer is a function of the transmit source level (due to transmit power, projector efficiency, and directivity), range and pathloss (due to absorption, spreading loss, and directivity), and the properties of the harvesting transducer (efficiency, directivity and sensitivity). Specifically, the RMS open-circuit voltage (V_{oc}) can be expressed as [3, 2]:

$$V_{oc} = 10^{\frac{RL(P_t,f,R)+RVS}{20}}$$

where RVS is the receiving voltage sensitivity of the backscatter node's transducer, and RL is the received signal level at the transducer, which itself is a function of the transmit power (P_t), transmit efficiency (η_{Tx}), range (R), and directivity of the projector (DI_{Tx}), spreading factor (k), and absorption coefficient (α) as per the following equation [3, 6]:

$$RL(P_t, f, R) = 170.8 + 10log(\eta_{Tx}P_t) + DI_{Tx} - k.10log(R) - \alpha(f)R$$

3.1.2 Harvested Voltage

The harvested voltage is a function of the open-circuit voltage (V_{oc}). In particular, recall that the harvesting transducer's output (after matching) is passed through a multi-stage rectifier that converts the AC to DC voltage and passively amplifies the voltage. The harvested voltage at output of the rectifier (V_{rect}) is a function of the number of stages (N) and the diode threshold voltage (V_{th}), and can be expressed as follows [35]:

$$V_{rect} = N(\sqrt{2}V_{oc} - V_{th})$$

In our prototype implementation, RVS = -180dB re 1V/μPa, $\eta_{Tx} = 0.175$, $P_{Tx} = 25$ W, $DI_{Tx} = 2.62$dB, $k = 1.5$, $\alpha = 0.0022$dB, $N = 4$, and V_{th}= 0.35 V.

To study the harvested voltage constraint in our battery-free imaging system, we simulate the rectified voltage as a function of range following the above model (fig-

ure 3-1a). The figure also plots the minimum activation voltage (dashed horizontal line), which corresponds to 3.2 V in our design. We consider three optimizations for our proof-of-concept prototype, following the parameters highlighted in prior work on underwater backscatter [2]. First, we consider a design whose harvesting transducers have an RVS of -157dB re 1V/μPa (instead of -180dB re 1V/μPa), and plot the rectified voltage (in blue). Our second optimization considers a projector whose efficiency is 0.5 (instead of 0.175), and we plot the corresponding rectified voltage (in orange). Finally, we study how increasing the transmit power from 25 W to 500 W impacts the harvested voltage as a function of range (in black). The figure shows that with more optimized engineering parameters, the range of an underwater battery-free imaging system may increase to more than 300 meters, matching prior analytical model [2].
It is worth noting that the activation voltage is also function of our system design parameters. In principle, the main limitation on the voltage is determined by the non-linearity of the harvester electronics, specifically the diodes, whose threshold voltage is 0.35V. One can approach this threshold voltage (and achieve higher ranges) by increasing the number of stages in the multi-stage rectifier as well as by using rectifiers with lower threshold voltages [8].

3.1.3 Harvested Power

Next, we analyze the harvested power as a function of range. The harvested power (P_{harv}) is a function of the open-circuit voltage, harvesting circuit efficiency (η_{harv}), and transducer impedance (Z) as per the following equation [3, 2]:

$$P_{harv} = \frac{\eta_{harv} V_{oc}^2 . Re(Z)}{\|Z\|^2}$$

In our prototype implementation, $\eta_{harv} = 0.16$ and $Z = 35$ - 203j.
We plot the harvested power as a function of range following the same parameters of the above model in (figure 3-1b). We also plot the minimum power (dashed horizontal line) required for our prototype to operate continuously. The plot demonstrates

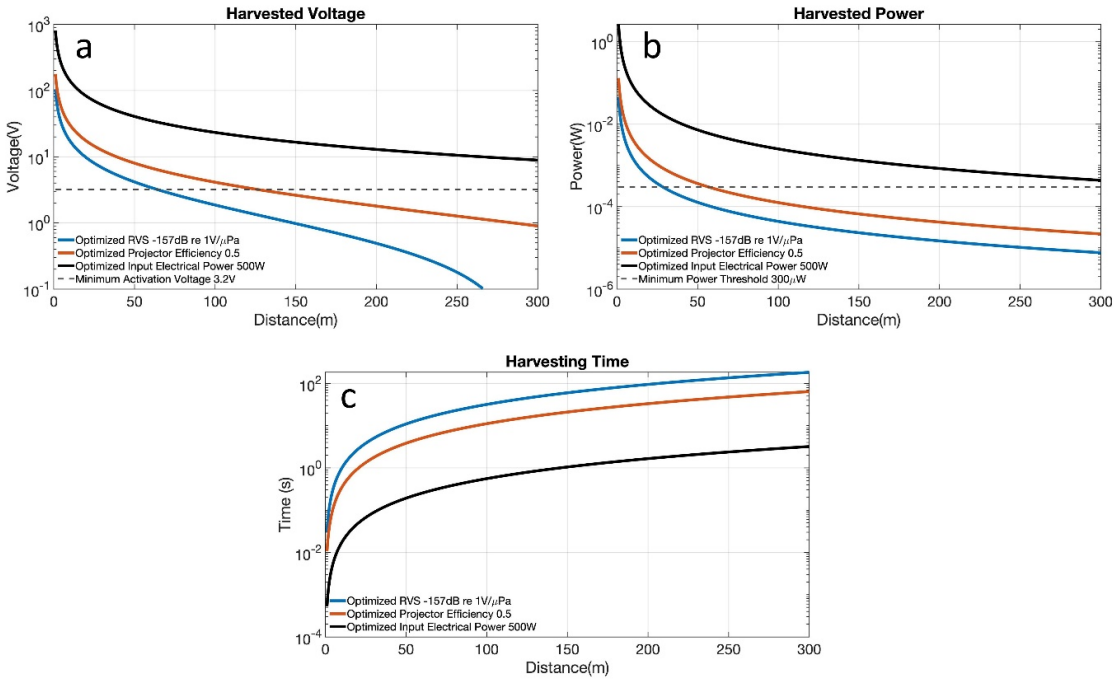

Figure 3-1: **Range analysis for the camera prototype.** (a) shows the rectified voltage as a function of the distance between the transmitter and the battery-free camera prototype. (b) shows the harvested electrical power plotted as a function of the distance between the transmitter and the battery-less camera prototype. (c) shows the harvesting time as a function of distance.

that underwater battery-free imaging may be possible at hundreds of meters under optimized engineering design parameters.

It is worth noting that the harvested power can be further improved by optimizing two other design parameters. First, in addition to the parameters discussed above, it is possible to boost the AC-to-DC power conversion efficiency from 0.16 to higher realizable efficiency of 0.60 [55]. Second, the end-to-end power transfer efficiency (and range) may be improved by using beamforming.[1] In particular, past work has considered underwater acoustic beamforming and demonstrated that it can enable directivity gains of 16dB [58]. A natural question here is: how can a projector identify the optimal beamforming direction so that it may electronically steer its array accordingly? If the backscatter node's location is known a priori, then the beam-

[1]Note that the current transducer has a toroidal radiation pattern (see Section 4.1). Beamforming would allow the projector to focus the energy in a specific direction thereby extending the range of operation for a given input power.

steering direction may be computed geometrically and the projector can apply the corresponding beamsteering vector. Alternatively, if the backscatter node's location (or the projector's location) is unknown, then the projector can find the correct beam by employing one of the standard beam searching algorithms [52, 25]. For example, the projector can first scan different directions, by sequentially applying different beamforming vectors. When it reaches the correct direction, the backscatter node powers up and responds with stored bits. The projector uses this feedback to identify the correct direction, and continues beamforming in that direction for the remainder of the communication session. Since the transmit source level in our evaluation is already high (180dB re:1μPa), such optimized designs will be critical to achieve higher range in future work.

3.2 Timing Analysis

In this section, we analyze the timing performance of our ultra-low-power imaging platform. Specifically, we analyze the time that the system needs to harvest sufficient energy to power up and the time needed to capture and communicate one full image.

3.2.1 Energy Harvesting Time

Our battery-free camera sensor operates entirely on the harvested power, and the time, T needed to harvest sufficient energy to capture a gray-scale image is given by the following equation:

$$T = \frac{1.4006mJ}{P_{harv}}$$

where $1.4006mJ$ is the energy required during the image capture phase (see table 2.2) and P_{harv} is the harvested power. The harvested power depends on the transmit power, distance from the projector, harvesting transducer's RVS, and the efficiency of the harvesting circuit. With our current design parameters (see Range Analysis), it takes around 10-12 seconds to harvest sufficient energy at 1 meter. However, recall from our discussion in Range Analysis that these parameters can be optimized to

increase the harvested power which would reduce the time needed to harvest sufficient energy. Specifically, using the model parameters mentioned in Range Analysis and the equation given above, we plot the harvesting time, T as a function of distance (figure 3-1c). The plot shows that under optimized design parameters, the energy harvesting time is less than a second (i.e., the imaging operation starts instantaneously) even beyond 100 meters.

Recall that sending a full image typically requires multiple captures (due to the memory limitations on the FPGA), and one might wonder whether each of these captures requires the above-mentioned harvesting time. However, that is not the case, and the sensor needs the harvesting time only once during the beginning of the operation. To see why, recall that the system operates in two phases: image capture phase and backscatter communication phase. The backscatter communication phase consumes significantly less power of 59 μW (table 2.2) and lasts longer (due to the narrow bandwidth of the underwater acoustic channel). As a result, the capacitor fully recharges during this phase before it needs to enter the image capture phase again, allowing for uninterrupted operation after the initial harvesting cycle.

Finally, it is worth noting that the above analysis assumes that the system is operating in warm start (i.e., there is some pre-stored charge across the capacitor). During the cold-start phase (which occurs only once in the system's lifetime), the capacitor is fully discharged and the time required to harvest sufficient energy to initiate the operation is given by:

$$T = \frac{\frac{1}{2}CV_{thres}^2}{P_{harv}}$$

where C is the capacitance value (7500 μF) and V_{thres} is the threshold voltage (3.2 V) across the capacitor needed to initiate the operation. With our current design parameters, it takes 4-5 minutes to harvest sufficient energy at 1 meter to initiate the imaging operation. Moreover, following the same analysis discussed above, optimizing the system design parameters would allow reduce this initiation time to few seconds.

3.2.2 Image Framerate

The framerate of our system depends on the time needed to capture and communicate image data to a remote receiver. Specifically, the total time, T, needed for one full image is given by the following equation:

$$T = (T_{segment} + \frac{Bits_{segment}}{Datarate}).Total_{segments}$$

Where $T_{segment}$ is the time needed to capture and store an image segment in the FPGA's memory and it is equal to 0.7 seconds (table 2.1), $Bits_{segment}$ is the total number of bits in a segment (25000 bits, which includes the bit-equivalent silent period, see FPGA Control and Logic in Methods), $Datarate$ is the bitrate of backscatter communication (recall that we used 1 kbps in our experiments), and $Total_{segments}$ is equal to the total number of segments (53 segments) in one full image (see FPGA Control and Logic in Methods). For a communication data rate of 1 kbps, it takes 1362.1 seconds (22.7 mins) to capture a grey-scale image and around 68 min to capture a color image. Note that the image transmission is the most time-consuming part because of the low datarate, and the framerate of the system can be improved by increasing the datarate of communication.

To achieve higher framerate, we successfully experimented with communicating at 5 kbps (with BERs of 10^{-3} at 1m). At such datarates, the time needed to capture and communicate a grey-scale image reduces to 5 mins (14 mins for the color image). Moreover, higher framerates are achievable by leveraging past work on underwater backscatter node design which has demonstrated throughputs up to 20kbps [21]; using such designs would further reduce the time for a grey-scale image to 1.1 mins (3.4 mins for a color image).

Chapter 4

Fabrication & Evaluation

4.1 Fabrication Methods

The underwater camera is attached to two piezoelectric transducers. The fabrication process of these transducers is similar to previous methods of building transducer nodes for underwater communication [29, 21]. Each underwater transducer contains two different types of piezoceramic cylinders (figure 4-1). The outer piezoceramic cylinder has an outer radius of 27mm, inner radius of 23.5mm, height of 40mm, and a nominal resonance frequency of 17 kHz in radial mode (SMC5447T40111, Steminc), while the inner piezoceramic cylinder has an outer radius of 18mm, inner radius of 15.5mm, height of 20mm, and a nominal resonance frequency of 30 kHz in radial mode (SMC3631T20111, Steminc). We stacked two of the inner piezoceramic cylinders and soldered them together to obtain the same height as that of the outer cylinder. We laser cut polyurethane gaskets from an abrasion-resistant polyurethane rubber sheet (40A, McMaster-CARR) and set them on 3D-printed (Creator Pro, Flashforge) end caps, and we tightly screwed the entire structure together to prevent leakage. We placed this entire structure inside a 3D printed cylindrical mold with 3.0 cm radius and 7.5 cm height, and we poured a polyurethane mixture (WC-575A/B, BJB Enterprises) into the mold to insulate it from the surrounding environment. The top and base lids have openings in between the outer and inner cylinders which allow the mixture to fill in the gaps between the cylinders. Afterwards, we placed this structure

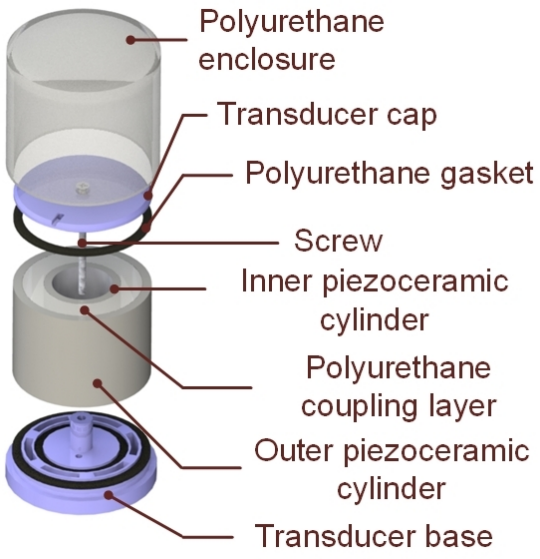

Figure 4-1: **Exploded view of the layered transducer.** The structure contains a polyurethane layer which is sandwiched between piezoceramic cylinders. The outer piezoceramic cylinder has a nominal resonance frequency of 17kHz, while the inner piezoceramic cylinder has a nominal resonance frequency of 30 kHz. Top and base caps are padded with polyurethane gaskets, and the entire structure is tightened with a screw, then encapsulated with another layer of polyurethane.

inside a pressure chamber (Pressure Chamber, Smooth-On) for 12 hours at a pressure of 60 psi to remove residual bubbles from the polyurethane solution. After removing the node from the pressure chamber, we manually removed the mold. We used this procedure to fabricate the transducers for both the projector and the camera. We simulated the beam pattern and directivity of these transducers using COMSOL Multiphysics (COMSOL). The transducers have a toroidal radiation pattern with a directivity index (DI) of 2.62 dB (figure 4-2).

The housing of the camera prototype consists of two dome structures (figure 4-3). The larger dome is six inches in diameter (6" Dome Port Lens, TELESIN) and houses the circuitry. The smaller dome comprises of an in-house built plastic base, an abrasion-resistant polyurethane rubber sheet, an acrylic dome which is 3 inches in diameter (Plastic Hemisphere, SupremeTech), and six screws to hold the entire structure together.

The electrical components of the design include a PCB (designed using a freely available software (Eagle, Autodesk) sent for fabrication to a commercial vendor

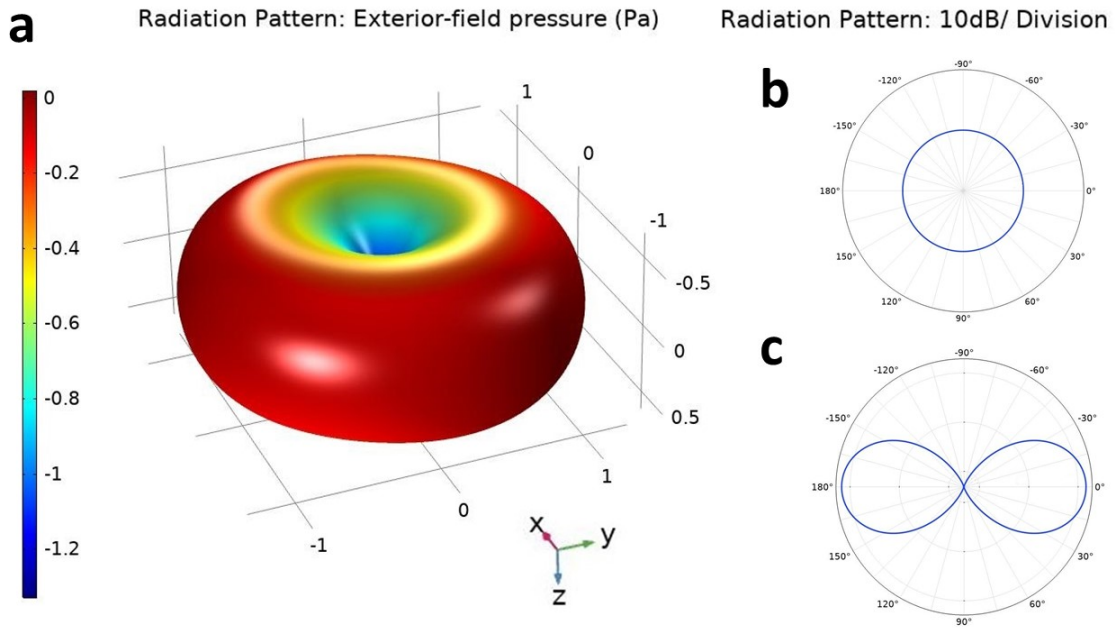

Figure 4-2: **Directivity of the layered transducer.** (a) shows the pressure radiation heatmap of the layered transducer obtained using COMSOL Multiphysics software. Dark blue regions correspond to low pressure, while dark red regions represent higher pressure. The layered transducer has a directivity index of 2.62 dB (b) shows the transverse cut of the radiation pattern which demonstrates that the layered transducer is omnidirectional in the horizontal plane. (c) shows the lateral cut of the radiation pattern.

(EasyPCBUSA, Sun Circuits)), an FPGA (IGLOO nano AGLN060, Microsemi), a CMOS monochrome camera sensor (HM01B0, HiMax), a camera connector (609-4320-2-ND, Digikey), two oscillators of 32 kHz (SiT1566AI-JV-18E-32.768E, SiTime) and 4 MHz (SiT8021AI-J4-18S-4.000000E, SiTime) frequencies, a 7500 μF supercapacitor (667-EEU-FS0J752S, Mouser Electronics), a 2.8 V voltage regulator (TPS7A03-28PDBVR LDO, Texas Instruments), a DC-DC step down converter (TPS62841DLCR, Texas Instruments) and red, green, and blue LEDs (604-WP154A4SUREQBFZG, Mouser Electronics). Additional components include four schottky diodes of 0.35 Volt threshold (750-CDBU0130L, Mouser Electronics), four capacitors of 0.1 μF value (587-3502-1-ND, Digikey), three other capacitors of values 47 μF (490-10559-1-ND, Digikey), 10 μF (810-CGA3E1X7T0G106M0, Mouser Electronics), and 4.7 μF (80-C0603C475M9P7411, Mouser Electronics), four resistors of 1 MΩ, two resistors of 4.7 kΩ (13-RE0603FRE074K7LCT-ND, Digikey), one 2.2 μH inductor (118-CC453232A-

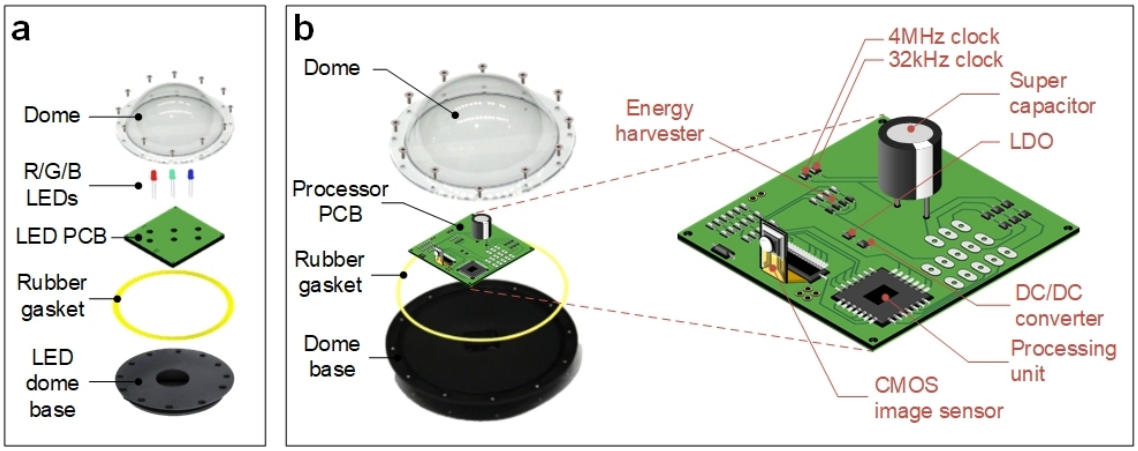

Figure 4-3: **Exploded view of the camera dome and LED dome.** (a) The LED dome contains the red (R), green (G), and blue (B) LEDs, and a layer of polyurethane gasket is added to the dome base to make it water-proof. (b) The camera PCB contains the Himax image sensor, supercapacitor for harvesting energy, power management electronics, and an FPGA for processing and memory. It also contains programming pins to program the FPGA and change camera parameters. The PCB is enclosed in a transparent dome, and the entire structure is tightly screwed to make it water-proof.

2R2KLTR-ND, Digikey), and six 750 μH inductors (HM3341-ND, Digikey). Each electrical component is individually tested and manually soldered using a digital hot air rework and soldering station (AO888A, Aoyue). Power measurements of electrical components were made using a power profiler (PPK2, Nordic Semiconductor).

A function generator (SGD 1032x, Siglent) connected to a fabricated piezoelectric transducer (fabrication procedure described above) through an audio amplifier (XLi 3500, Crown) is used as an underwater projector to transmit acoustic signals. An acoustic hydrophone (H2A, Aquarian) is used as a remote receiver to measure underwater sound. The hydrophone is connected to a laptop (XPS 15 7590, Dell), which records sound using an open-source audio recording software (Audacity) at a sampling rate of 192,000 samples/sec. The signal processing and decoding algorithms are implemented in MATLAB R2020b (Mathworks). The FPGA program is designed using a freely available IDE (Libero SoC v11.9, Microsemi), and the IDE-generated programming file is flashed on the FPGA using a programmer kit (FlashPro 3, Microsemi).

4.2 Cost Analysis

The total cost of fabricating and assembling our underwater batteryless imaging sensor prototype is $353.97 (table 4.1). The main components of the design are the

Device Components	Quantity	Cost ($)
Piezo Ceramic Cylinder (17 kHz)	2	91.50
Piezo Ceramic Cylinder (30 kHz)	4	140.00
Polyurethane Elastomer WC-575 A/B	1 (0.03 Gallon)	4.34
HiMax HM01B0 Camera Sensor	1	9.95
IGLOO nano AGLN060 FPGA	1	12.72
TELESIN 6" Dome Port	1	45.00
SupremeTech Acrylic 3" Dome Hemisphere	1	10.99
PCB Fabrication	1	12.00
Inductors HM3341ND	6	18.98
Electrical Components (including Oscillators, Capacitors, Resistors, Diodes)	-	19.48
	Total Cost	**$353.97**

Table 4.1: **Cost breakdown of battery-free underwater camera prototype.** This table shows the cost breakdown of the underwater battery free imaging prototype. The overall cost of building a battery-free imaging sensor is $353.97.

piezoceramic transducers, camera sensor, FPGA, PCB, and housing. The prototype uses a total of six piezoceramic cylinders: two with a resonance frequency of 17 kHz and four with a resonance frequency of 30 kHz. The total cost of the piezoceramic cylinders is $231.5 (45.7*2 +35*4). The housing of the camera prototype consists of a Telesin dome port which costs $45 and a smaller acrylic dome priced at $11 to encapsulate the active illumination hardware. The IGLOO nano FPGA costs $12.72, the Himax camera sensor costs $9.95, and the total cost of PCB fabrication is $12. The low cost of fabrication of our batteryless prototype - coupled with the fact that it does not require an extensive infrastructure in the form of cabling for power and communication [32, 48, 60, 36] - makes underwater backscatter imaging a viable method for scalable underwater imaging.

4.3 Evaluation & Testing

The batteryless camera prototype was evaluated qualitatively and quantitatively in enclosed and open water environments.

4.3.1 Enclosed Water Testing Environments

Imaging: Testing in controlled environments was performed in an enclosed water tank with a depth of 1.5 m and rectangular cross section of 3 m x 4 m (figure 4-4). Here, the projector, hydrophone, and the two transducers of the batteryless camera (for harvesting and backscatter) were all submerged at a depth of 75 cm below the water surface. At the same time, the domes housing the camera and illumination (which are connected to the two transducers using wires) were placed along with the underwater objects in a separate tank to isolate them and control environmental conditions including lighting and nutrient levels. Specifically, the coral reef model and the *Protoreaster linckii* were co-located with the camera at the base of a smaller tank with a depth of 40 cm and a rectangular cross-section of 40 cm x 50 cm (figure 4-4). Similarly, several seeds of *Aponogeton ulvaceus* were planted in freshwater aquarium substrate in a third tank with the same dimensions (40 cm x 50 cm x 40 cm), and the camera was used to monitor their growth over a period of one week. Images in figures 1-2b, 1-3c, and 1-3d demonstrate successful imaging in these evaluation scenarios.

AprilTag Detection and Localization: We used the imaging method to detect and localize Apriltags(figure 4-5a) in underwater environments. Figure 4-5b shows an image of an AprilTag obtained using underwater backscatter imaging. Figure 4-5c shows the detection accuracy and the localization distance of the AprilTags imaged at different ranges. The results demonstrate very high detection rate and high localization accuracy (localization error below 10 cm) up to 3.5 m. Beyond this range, the current resolution of the CMOS imaging sensor limits both detection and localization; longer detection ranges would be possible with higher-resolution sensors.

AprilTag Data Collection: Data collection for the AprilTag localization and de-

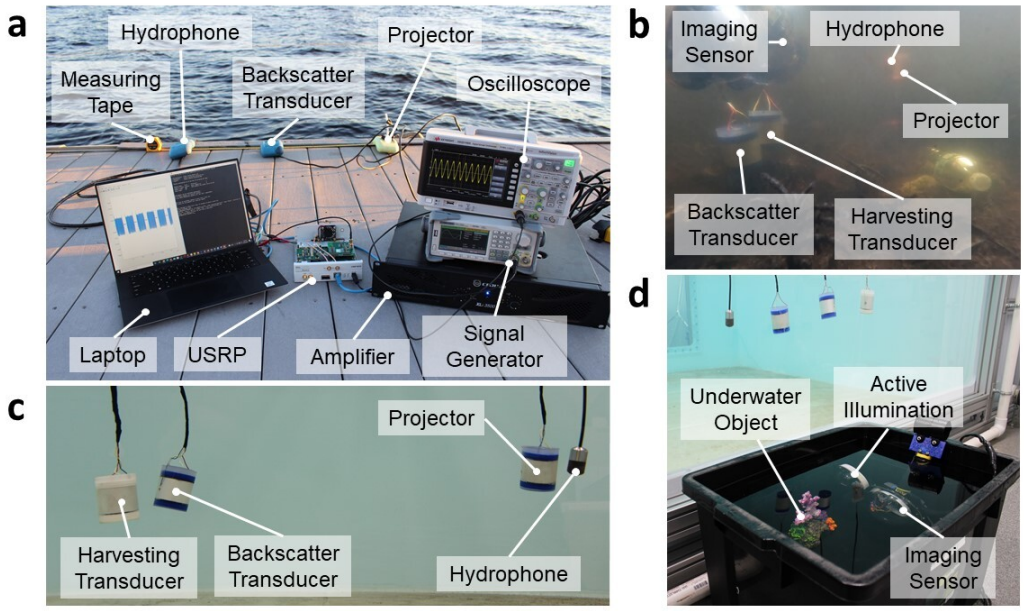

Figure 4-4: **The prototype evaluation in enclosed and open environments.** (a) shows the experimental setup in Charles River, MA. (b) shows the underwater setup in Keyser Pond, NH. (c) shows the nodes placed in the larger enclosed tank in the lab. (d) shows the experimental setup while imaging in the smaller external tank.

tection task was performed in the larger tank (3 m x 4 m x 1.5 m). For this task, the camera sensor was submerged in the tank at a depth of 30 cm below the surface and placed at one side of the tank to capture images of the AprilTag. The AprilTag was submerged at the same depth. The experimental trial was repeated by placing the AprilTag at 8 different locations separated by 50 cm, up to 4 m of maximum range between the AprilTag and the camera (i.e., the edge of the enclosed tank). At each location (i.e., range), we used the camera to capture 20 images of the AprilTag, where the orientation and angle was varied with respect to the camera in each image, resulting in a total of 160 images (figure 4-6). To speed up the data collection process, these images were collected by connecting the FPGA output directly to a USRP N210 software radio (Ettus); this removes the bandwidth limitation of underwater acoustic communication and enables programming the FPGA to transmit captured pixels at a much higher rate (2 Mbps). Note that we did not bypass the FM0 backscatter modulation for the results shown in Figure 4-5c, but only bypassed the underwater channel. In addition to this data collection, Figure 4-5b shows a sample AprilTag

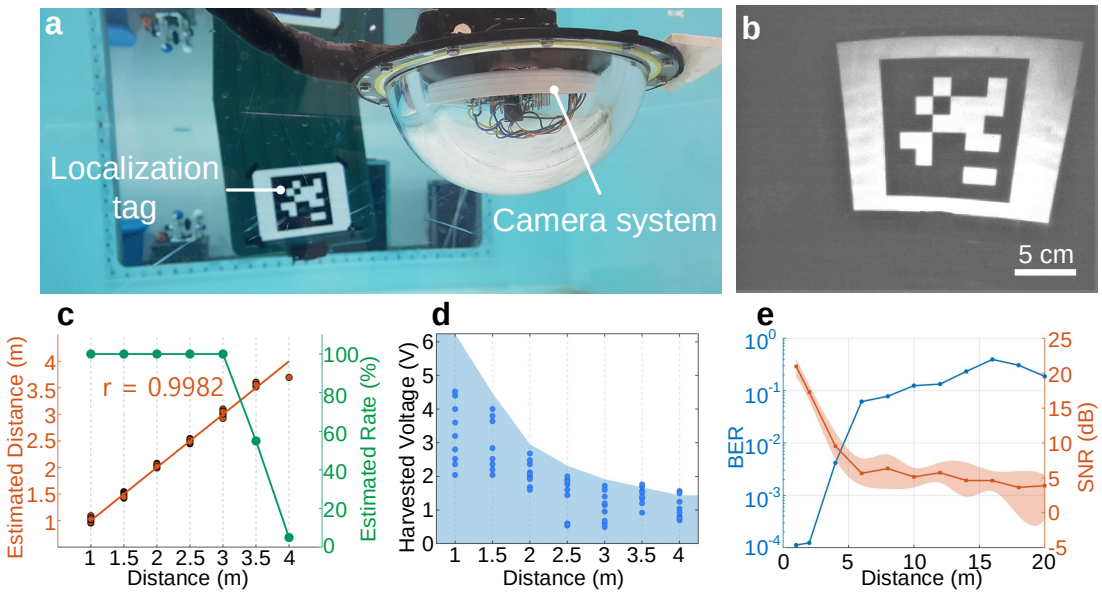

Figure 4-5: **Captured images of AprilTag markers demonstrate successful underwater inference and localization.** (a) The prototype was used to detect and localize submerged localization tags. (b) An image of the AprilTag obtained using a batteryless prototype. (c) The estimated location of the AprilTag is plotted in red as a function of its actual location, and the detection rate of AprilTag is plotted in green as a function of distance. (d) Harvested voltage is plotted as a function of distance between the transmitter and the batteryless camera prototype. The dots indicate the voltage at depths, while the contour indicates the maximum voltage obtained when the node's depth is varied over the entire water column at the corresponding distance. (e) SNR and BER of the imaging method are plotted as a function of distance. The lower and upper bound of the orange band around the SNR plot indicate the 10th and 90th percentile of the collected SNR data at the corresponding distance. The dotted and solid lines show the BER of the imaging method before and after equalization respectively.

image captured in this setup using end-to-end batteryless imaging and underwater backscatter communication (at 1 kbps).

Calibration for AprilTag Localization: In order to determine an accurate relationship between a 3D location in the environment and its corresponding 2D pixel in the image captured by our underwater camera, we compute the 3 x 3 homography matrix that contains all the physical information (location and orientation) of the tag [18]. Computation of the matrix requires the intrinsic parameters of the camera, such as the focal length and optical center of the camera. To extract the parameters from our underwater camera, we used a checkerboard calibration method, which is

standard in 3D reconstruction problems in computer vision [18]. We captured 150 images of the checkerboard (7x10 square pixels with a pixel size of 23 mm x 23 mm) from different viewpoints at 3 different distances: 50 cm, 80 cm, and 120 cm and extracted the intrinsic parameters using the Multiplane calibration algorithm [66]. This calibration process needs to be completed only once since we used the same underwater camera throughout all of the measurements.

After the camera is calibrated, the detection and localization tasks are performed on the captured AprilTag images in the dataset described earlier. The tasks were performed following similar procedures to prior work on AprilTag localization [43]. The detection algorithm computes the gradient of every pixel and clusters the pixels that have similar direction and magnitude into components. After performing a recursive depth-first search, it extracts the edges of the AprilTag. Using the edges, the algorithm finds four-sided regions that have a darker interior than their exterior and verifies if the region has valid tag pixels. If the pattern is valid, the detection succeeds, and the region is used as an input to the homography matrix which outputs the tag's location.

4.3.2 Open Water Testing Environments

Open water testing of the prototype was performed in Keyser Pond, NH and in Charles River, MA (figure 4-4a and figure 4-4b). In Keyser Pond, the acoustic transmitter[1], harvesting and backscatter transducers, and hydrophone were submerged half a meter below the water surface and the camera sensor was placed at a distance of 50 cm from the plastic water bottle. The image was collected at night, yet the prototype was successfully able to capture color features (as shown in figure 1-3b in the introduction) due to its active illumination method.

Long-range communication experiments were performed in the Charles River. We

[1]In the Keyser Pod experiment, the cumulative sound exposure level (SEL_{cum}) value was 191.29 dB re 1 μPa^2s at a distance of 10 meters from the transmitter. Note that this value is within the limits defined by Marine Mammal Protection Act (MMPA) [49] for all marine mammals except for mammals that lie within high-frequency cetacean hearing group. However, there were no mammals from this group (or any other group) within the 10-meter radius of the transmitter

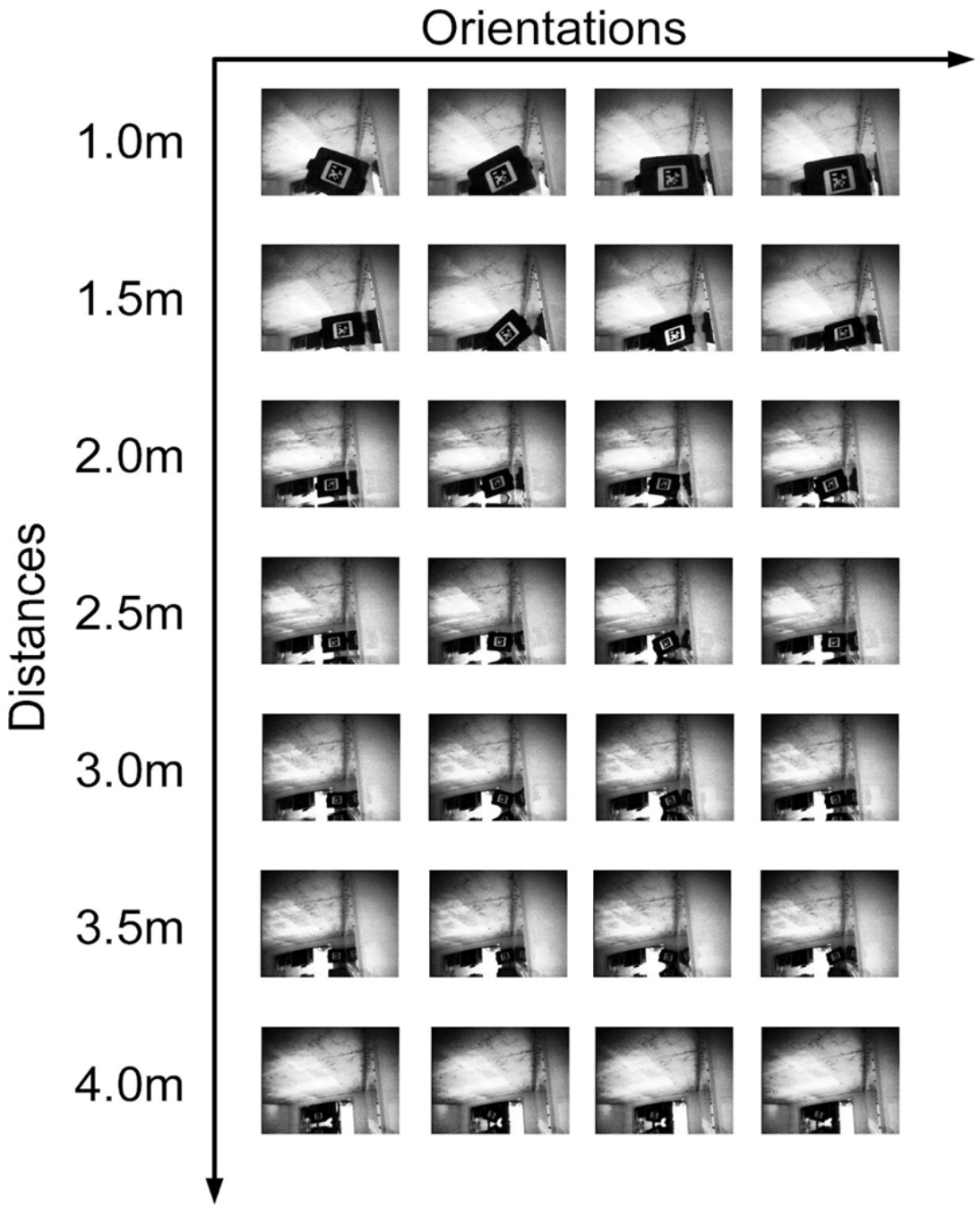

Figure 4-6: **Sample AprilTag images**. The camera prototype was used to capture a total of 160 AprilTag images at different distances, orientations, and angles.

tested the method's ability to communicate with a hydrophone receiver at different distances, and computed the signal-to-noise ratio (SNR) and the bit error rate (BER) of the decoded packets at different distances (figure 4-5e). The plot shows that SNR decays and the BER increases with distance, demonstrating the ability to robustly

decode packets beyond 40 meters by leveraging a decision feedback equalizer at the receiver [20]. In these experiments, the acoustic projector[2], harvesting and backscatter transducers, and hydrophone were all submerged at a depth of 2 m below the water surface. The projector and the backscatter transducer were separated by a distance of 50 cm and the hydrophone was moved further away up to 40 m to test communication at different distances. For this experiment, the backscatter node was programmed to communicate a known pseudo-random sequence of 50 bits (10 bits of preamble with 40 bits of data) in each packet at a data rate of 1 kbps. These bits were constructed in MATLAB and were fed to the transistor switches M1 and M2 using a signal generator (figure 2-2). The hydrophone was connected to a USRP N210 to record the received signal for 20 seconds, resulting in 400 packets. For each distance, we recorded data at three different depths (1.5 m, 2 m, and 2.5 m), and for each depth, we computed a single value for BER and different values for SNR (one for each decoded packet). The BER value was computed over all packets by comparing the decoded 50 bits of each packet with the actual transmitted bits. SNR values were computed individually for each packet where the signal power was determined by projecting the received packet onto the transmitted packet and noise power was evaluated by subtracting the signal power from the total received power. The SNR and BER curves are shown in figure 4-5e as a function of distance, where the BER curve shows the median value of BER across all three depths and the solid line for SNR represents the median SNR over 900 packets (300 packets * 3 depths). The lower and upper bound of the shaded region for the SNR curve represent the 10th and 90th percentile respectively.

In addition to testing the communication capabilities of our method, we also evaluated its harvesting performance at different ranges. An experiment was performed in the Charles River, where the acoustic projector and the harvester node were submerged at a depth of 2 m below the water surface. The harvester node was moved further away (with an interval of 50 cm) up to 4 m. The open-circuit, rectified, harvested

[2]In our experiments at Charles River, SEL_{cum} value was 168 dB re 1 μPa^2s at a distance of 10 meters from the transmitter. This SEL_{cum} value is within the MMPA acoustic thresholds for all marine mammal hearing groups.

voltage was measured using a digital oscilloscope. For each distance, the harvester node was moved to three different depths (1.5 m, 2 m, 2.5 m) and the voltage was measured at each depth. At each depth, 3 measurements were taken, resulting in a total of 9 measurements at each range. The harvester node was also moved gradually across the entire water column for each distance to measure the maximum voltage that the harvester transducer can harvest at each distance. The plot for harvested voltage as a function of distance is shown in figure 4-5d where the maximum harvested voltage is represented as the contour of the shaded region and the 9 measurements at 3 different depths are represented as dots.

Chapter 5

Discussion & Conclusion

We discuss the performance of our underwater wireless imaging method in the context of alternative methods for underwater communication.

5.1 Comparison to Low-Power Acoustic Modems

Our imaging method leverages acoustic backscatter communication to communicate image data at net-zero power. Our evaluation demonstrates that the method achieves communication ranges that are comparable to state-of-the-art low-power underwater modems, albeit at much lower power. Specifically, a state-of-the-art low-power acoustic modem [50] requires 80 milli-Watts to transmit data at 1 kbps over 100m, while our prototype consumes 59 microwatts to transmit data at the same rate over 40m (see figure 4-5e, and see Backscatter Communication Phase in table 2.1). Our analysis demonstrates that higher ranges are realizable with more optimized transducers (see Section 3.1).

One might wonder whether prior low-power modems could be operated entirely based on harvested acoustic energy and used for net-zero-power underwater imaging. To answer this question, we consider the amount of time needed to harvest sufficient energy to transmit an image using a state-of-the-art low-power modem. Since the modem operates at the same data rate as our backscatter prototype, it would require the same amount of time for image transmission (1362.1seconds, see table 2.2)

to capture and transmit a grayscale image. Multiplying this by the communication power (80mW) results in 106.07 Joules, which is 594x higher than our backscatter-based wireless platform. If one were to harvest this energy from an acoustic source (which can typically provide a few hundreds of microwatts, see Section 3.1), it would take 4-6 days to harvest sufficient energy before initiating an imaging operation (in comparison to our power-up time of 10-12 seconds). Thus, it would be impractical to design an underwater battery-free wireless imaging system leveraging prior low-power underwater acoustic modems.

Here, it is worth noting that backscatter communication does not eliminate the energy requirements altogether; instead, it shifts the burden of power consumption from the backscatter node to a remote acoustic source (which could be on a drone, submarine, ship, or coastal base station) with a dedicated power source. According to the range analysis in prior work [2] (see Section 3.1), acoustic backscatter can operate at distances of hundreds of meters under optimized system design parameters. Hence, with careful engineering design, it would be possible to leverage underwater backscatter sensor nodes for low-cost, scalable undersea observations.

5.2 Comparison to Alternative Underwater Communication Technologies

Next, we compare underwater acoustic backscatter to alternative underwater wireless communication modalities that do not leverage acoustic signals [51, 22]. Underwater optical communication systems can achieve higher data rates than acoustic communication systems (up to Gbps), but their range is limited by the turbidity of water [51]. Specifically, the communication range of low-power optical modems is less than 10 meters in turbid waters [45, 15], in contrast to hundreds of meters (or kilometers) for underwater acoustic communications [51] (including underwater acoustic backscatter [2]). Aside from optical communications, some underwater communication systems use radio frequency signals, such as very-low-frequency (VLF)

and extremely-low-frequency (ELF); these systems can achieve underwater communication up to few kilometers, but require kilometer-long antennas [37], which makes them bulky, expensive, and impractical for a compact underwater imaging system. Finally, researchers have considered higher-frequency RF communication technologies for underwater communication (such as Bluetooth or WiFi), but these are limited to a few tens of centimeters of range [54], making them undesirable for underwater communication.

In summary, our evaluation and analysis demonstrate that acoustic backscatter is a viable approach for low-cost, low-power, and long-range imaging of underwater environments. Fundamentally, the power asymmetry inherent to acoustic backscatter communication makes it a desirable approach for underwater sensor nodes, and enables the design of batteryless underwater cameras that could be used for long-term in situ sensing of the underwater world.

Bibliography

[1] Sayed Saad Afzal, Reza Ghaffarivardavagh, Waleed Akbar, Osvy Rodriguez, and Fadel Adib. Enabling higher-order modulation for underwater backscatter communication. In *Global Oceans 2020: Singapore–US Gulf Coast*, pages 1–6. IEEE, 2020.

[2] Alper Bereketli. Interference-free source deployment for coverage in underwater acoustic backscatter networks. *Peer-to-Peer Networking and Applications*, 15(3):1577–1594, 2022.

[3] Alper Bereketli and Semih Bilgen. Remotely powered underwater acoustic sensor networks. *IEEE Sensors Journal*, 12(12):3467–3472, 2012.

[4] Aggelos Bletsas, John Kimionis, Antonis G Dimitriou, and George N Karystinos. Single-antenna coherent detection of collided fm0 rfid signals. *IEEE Transactions on Communications*, 60(3):756–766, 2012.

[5] Michael J Buckingham, Broderick V Berknout, and Stewart AL Glegg. Imaging the ocean with ambient noise. *Nature*, 356(6367):327–329, 1992.

[6] John L Butler and Charles H Sherman. *Transducers and arrays for underwater sound*. Springer, 2016.

[7] Michael H Carr, Michael JS Belton, Clark R Chapman, Merton E Davies, Paul Geissler, Richard Greenberg, Alfred S McEwen, Bruce R Tufts, Ronald Greeley, Robert Sullivan, et al. Evidence for a subsurface ocean on europa. *Nature*, 391(6665):363–365, 1998.

[8] Hyouk-Kyu Cha, Woo-Tae Park, and Minkyu Je. A cmos rectifier with a cross-coupled latched comparator for wireless power transfer in biomedical applications. *IEEE Transactions on Circuits and Systems II: Express Briefs*, 59(7):409–413, 2012.

[9] Yi Chao. Autonomous underwater vehicles and sensors powered by ocean thermal energy. In *OCEANS 2016-Shanghai*, pages 1–4. IEEE, 2016.

[10] Juan Chen, Caiming Sun, and Aidong Zhang. Autonomous navigation for adaptive unmanned underwater vehicles using fiducial markers. In *2021 IEEE International Conference on Robotics and Automation (ICRA)*, pages 9298–9304. IEEE, 2021.

[11] Erik E Cordes and Lisa A Levin. Exploration before exploitation, 2018.

[12] John B Corliss, Jack Dymond, Louis I Gordon, John M Edmond, Richard P von Herzen, Robert D Ballard, Kenneth Green, David Williams, Arnold Bainbridge, Kathy Crane, et al. Submarine thermal springs on the galapagos rift. *Science*, 203(4385):1073–1083, 1979.

[13] Corrado Costa, Michele Scardi, Valerio Vitalini, and Stefano Cataudella. A dual camera system for counting and sizing northern bluefin tuna (thunnus thynnus; linnaeus, 1758) stock, during transfer to aquaculture cages, with a semi automatic artificial neural network tool. *Aquaculture*, 291(3-4):161–167, 2009.

[14] Daniel A Duecker, Nathalie Bauschmann, Tim Hansen, Edwin Kreuzer, and Robert Seifried. Towards micro robot hydrobatics: Vision-based guidance, navigation, and control for agile underwater vehicles in confined environments. In *2020 IEEE/RSJ International Conference on Intelligent Robots and Systems (IROS)*, pages 1819–1826. IEEE, 2020.

[15] Mohammed Elamassie, Farshad Miramirkhani, and Murat Uysal. Performance characterization of underwater visible light communication. *IEEE Transactions on Communications*, 67(1):543–552, 2018.

[16] Aidan Fitzpatrick, Ajay Singhvi, and Amin Arbabian. An airborne sonar system for underwater remote sensing and imaging. *IEEE Access*, 8:189945–189959, 2020.

[17] United Nations Food and Agriculture Organization. Sustainable fisheries and aquaculture for food security and nutrition. https://www.fao.org/3/i3844e/i3844e.pdf, 2014.

[18] David Forsyth and Jean Ponce. Computer vision: A modern approach. always learning, 2012.

[19] Christian LE Franzke. Nonlinear climate change. *Nature Climate Change*, 4(6):423–424, 2014.

[20] Lee Freitag, Matt Grund, Sandipa Singh, and Mark Johnson. Acoustic communication in very shallow water: results from the 1999 auv fest. In *OCEANS 2000 MTS/IEEE Conference and Exhibition. Conference Proceedings (Cat. No. 00CH37158)*, volume 3, pages 2155–2160. IEEE, 2000.

[21] Reza Ghaffarivardavagh, Sayed Saad Afzal, Osvy Rodriguez, and Fadel Adib. Ultra-wideband underwater backscatter via piezoelectric metamaterials. In *Proceedings of the Annual conference of the ACM Special Interest Group on Data Communication on the applications, technologies, architectures, and protocols for computer communication*, pages 722–734, 2020.

[22] Camila MG Gussen, Paulo SR Diniz, Marcello LR Campos, Wallace A Martins, Felipe M Costa, and Jonathan N Gois. A survey of underwater wireless communication technologies. *J. Commun. Inf. Sys*, 31(1):242–255, 2016.

[23] Seongwon Han, Roy Chen, Youngtae Noh, and Mario Gerla. Real-time video streaming from mobile underwater sensors. In *Proceedings of the International Conference on Underwater Networks & Systems*, pages 1–8, 2014.

[24] Kevin Peter Hand and Christopher R German. Exploring ocean worlds on earth and beyond. *Nature Geoscience*, 11(1):2–4, 2018.

[25] Haitham Hassanieh, Omid Abari, Michael Rodriguez, Mohammed Abdelghany, Dina Katabi, and Piotr Indyk. Fast millimeter wave beam alignment. In *Proceedings of the 2018 Conference of the ACM Special Interest Group on Data Communication*, pages 432–445, 2018.

[26] Samuel V Hulse, Julien P Renoult, and Tamra C Mendelson. Sexual signaling pattern correlates with habitat pattern in visually ornamented fishes. *Nature communications*, 11(1):1–8, 2020.

[27] SRI International. Manta: Reliable and safe kite energy system. https://arpa-e.energy.gov/technologies/projects/manta-reliable-and-safe-kite-energy-system, 2020.

[28] Jules S Jaffe. Underwater optical imaging: the past, the present, and the prospects. *IEEE Journal of Oceanic Engineering*, 40(3):683–700, 2014.

[29] Junsu Jang and Fadel Adib. Underwater backscatter networking. In *Proceedings of the ACM Special Interest Group on Data Communication*, pages 187–199. 2019.

[30] Chien-Chi Kao, Yi-Shan Lin, Geng-De Wu, and Chun-Ju Huang. A comprehensive study on the internet of underwater things: applications, challenges, and channel models. *Sensors*, 17(7):1477, 2017.

[31] Kakani Katija, C Anela Choy, Rob E Sherlock, Alana D Sherman, and Bruce H Robison. From the surface to the seafloor: How giant larvaceans transport microplastics into the deep sea. *Science advances*, 3(8):e1700715, 2017.

[32] Kakani Katija, Rob E Sherlock, Alana D Sherman, and Bruce H Robison. New technology reveals the role of giant larvaceans in oceanic carbon cycling. *Science Advances*, 3(5):e1602374, 2017.

[33] Kakani Katija, Giancarlo Troni, Joost Daniels, Kelly Lance, Rob E Sherlock, Alana D Sherman, and Bruce H Robison. Revealing enigmatic mucus structures in the deep sea using deeppiv. *Nature*, 583(7814):78–82, 2020.

[34] Robert K Katzschmann, Joseph DelPreto, Robert MacCurdy, and Daniela Rus. Exploration of underwater life with an acoustically controlled soft robotic fish. *Science Robotics*, 3(16):eaar3449, 2018.

[35] Tony Kuphaldt. Lessons in electric circuits, volume iii–semiconductors, 2009.

[36] Katherine Lam, Robin S Bradbeer, Paul KS Shin, Kenneth KK Ku, and Paul Hodgson. Application of a real-time underwater surveillance camera in monitoring of fish assemblages on a shallow coral communities in a marine park. In *OCEANS 2007*, pages 1–7. IEEE, 2007.

[37] Marco Lanzagorta. Underwater communications. *Synthesis lectures on communications*, 5(2):1–129, 2012.

[38] Baosheng Li, Jie Huang, Shengli Zhou, Keenan Ball, Milica Stojanovic, Lee Freitag, and Peter Willett. Mimo-ofdm for high-rate underwater acoustic communications. *IEEE Journal of Oceanic Engineering*, 34(4):634–644, 2009.

[39] Bettina Meyer, Ulrich Freier, Volker Grimm, Jürgen Groeneveld, Brian PV Hunt, Sven Kerwath, Rob King, Christine Klaas, Evgeny Pakhomov, Klaus M Meiners, et al. The winter pack-ice zone provides a sheltered but food-poor habitat for larval antarctic krill. *Nature ecology & evolution*, 1(12):1853–1861, 2017.

[40] Camilo Mora, Derek P Tittensor, Sina Adl, Alastair GB Simpson, and Boris Worm. How many species are there on earth and in the ocean? *PLoS biology*, 9(8):e1001127, 2011.

[41] Andrew D Mullen, Tali Treibitz, Paul LD Roberts, Emily LA Kelly, Rael Horwitz, Jennifer E Smith, and Jules S Jaffe. Underwater microscopy for in situ studies of benthic ecosystems. *Nature Communications*, 7(1):1–9, 2016.

[42] Ivan Nagelkerken, Bayden D Russell, Bronwyn M Gillanders, and Sean D Connell. Ocean acidification alters fish populations indirectly through habitat modification. *Nature Climate Change*, 6(1):89–93, 2016.

[43] Edwin Olson. Apriltag: A robust and flexible visual fiducial system. In *2011 IEEE international conference on robotics and automation*, pages 3400–3407. IEEE, 2011.

[44] Melissa M Omand, Deborah K Steinberg, and Karen Stamieszkin. Cloud shadows drive vertical migrations of deep-dwelling marine life. *Proceedings of the National Academy of Sciences*, 118(32):e2022977118, 2021.

[45] Hassan Makine Oubei, Changping Li, Ki-Hong Park, Tien Khee Ng, Mohamed-Slim Alouini, and Boon S Ooi. 2.3 gbit/s underwater wireless optical communications using directly modulated 520 nm laser diode. *Optics express*, 23(16):20743–20748, 2015.

[46] Nicholas L Payne, Gil Iosilevskii, Adam Barnett, Chris Fischer, Rachel T Graham, Adrian C Gleiss, and Yuuki Y Watanabe. Great hammerhead sharks swim on their side to reduce transport costs. *Nature communications*, 7(1):1–5, 2016.

[47] Stephen C Riser, Howard J Freeland, Dean Roemmich, Susan Wijffels, Ariel Troisi, Mathieu Belbéoch, Denis Gilbert, Jianping Xu, Sylvie Pouliquen, Ann Thresher, et al. Fifteen years of ocean observations with the global argo array. *Nature Climate Change*, 6(2):145–153, 2016.

[48] Bruce H Robison, Kim R Reisenbichler, and Rob E Sherlock. The coevolution of midwater research and rov technology at mbari. *Oceanography*, 30(4):26–37, 2017.

[49] Joe Roman, Irit Altman, Meagan M Dunphy-Daly, Caitlin Campbell, Michael Jasny, and Andrew J Read. The marine mammal protection act at 40: status, recovery, and future of us marine mammals. *Annals of the New York Academy of Sciences*, 1286(1):29–49, 2013.

[50] Antonio Sanchez, Sara Blanc, Pedro Yuste, and Juan Jose Serrano. A low cost and high efficient acoustic modem for underwater sensor networks. In *OCEANS 2011 IEEE-Spain*, pages 1–10. IEEE, 2011.

[51] Giuseppe Schirripa Spagnolo, Lorenzo Cozzella, and Fabio Leccese. Underwater optical wireless communications: Overview. *Sensors*, 20(8):2261, 2020.

[52] Dongjin Seo, Hao-Yen Tang, Jose M Carmena, Jan M Rabaey, Elad Alon, Bernhard E Boser, and Michel M Maharbiz. Ultrasonic beamforming system for interrogating multiple implantable sensors. In *2015 37th Annual International Conference of the IEEE Engineering in Medicine and Biology Society (EMBC)*, pages 2673–2676. IEEE, 2015.

[53] Milica Stojanovic. On the relationship between capacity and distance in an underwater acoustic communication channel. *ACM SIGMOBILE Mobile Computing and Communications Review*, 11(4):34–43, 2007.

[54] Kay Strama, Daniel Weber, and Helge Renkewitz. Evaluation of wifi data transmission algorithms for short distance underwater communication. In *OCEANS 2021: San Diego–Porto*, pages 1–6. IEEE, 2021.

[55] Ahmadreza Tabesh and Luc G Fréchette. A low-power stand-alone adaptive circuit for harvesting energy from a piezoelectric micropower generator. *IEEE Transactions on Industrial Electronics*, 57(3):840–849, 2009.

[56] Masaya Tamura, Kousuke Murai, and Marimo Matsumoto. Design of conductive coupler for underwater wireless power and data transfer. *IEEE Transactions on Microwave Theory and Techniques*, 69(1):1161–1175, 2020.

[57] George W Taylor, Joseph R Burns, SA Kammann, William B Powers, and Thomas R Welsh. The energy harvesting eel: a small subsurface ocean/river power generator. *IEEE journal of oceanic engineering*, 26(4):539–547, 2001.

[58] Yong Wang, Yixin Yang, Yuanliang Ma, and Zhengyao He. Robust high-order superdirectivity of circular sensor arrays. *The Journal of the Acoustical Society of America*, 136(4):1712–1724, 2014.

[59] John Waterston, Jason Rhea, Scott Peterson, Leslie Bolick, Jennifer Ayers, and Jeffrey Ellen. Ocean of things: Affordable maritime sensors with scalable analysis. In *OCEANS 2019-Marseille*, pages 1–6. IEEE, 2019.

[60] Peter H Wiebe and Mark C Benfield. From the hensen net toward four-dimensional biological oceanography. *Progress in Oceanography*, 56(1):7–136, 2003.

[61] Nan Wu, Quan Wang, and XiangDong Xie. Ocean wave energy harvesting with a piezoelectric coupled buoy structure. *Applied Ocean Research*, 50:110–118, 2015.

[62] Tidal X. Tidal protecting the ocean while feeding humanity sustainably. https://x.company/projects/tidal/, 2021.

[63] Dana R Yoerger, Annette F Govindarajan, Jonathan C Howland, Joel K Llopiz, Peter H Wiebe, Molly Curran, Justin Fujii, Daniel Gomez-Ibanez, Kakani Katija, Bruce H Robison, et al. A hybrid underwater robot for multidisciplinary investigation of the ocean twilight zone. *Science Robotics*, 6(55):eabe1901, 2021.

[64] James Younce, Andrew Singer, Thomas Riedl, Blake Landry, Andrew Bean, and Toros Arikan. Experimental results with hf underwater acoustic modem for high bandwidth applications. In *2015 49th Asilomar conference on signals, systems and computers*, pages 248–252. IEEE, 2015.

[65] Qian Zhang, Qijie Liang, Dilip Krishna Nandakumar, Hao Qu, Qiongfeng Shi, Fuad Indra Alzakia, Darrell Jun Jie Tay, Lin Yang, Xueping Zhang, Lakshmi Suresh, et al. Shadow enhanced self-charging power system for wave and solar energy harvesting from the ocean. *Nature communications*, 12(1):1–11, 2021.

[66] Zhengyou Zhang. A flexible new technique for camera calibration. *IEEE Transactions on pattern analysis and machine intelligence*, 22(11):1330–1334, 2000.